

# Investigating high-performance sulfur–metal nanocomposites for lithium batteries

Vittorio Marangon<sup>1,†</sup>, Daniele Di Lecce<sup>2,†</sup>, Fabio Orsatti<sup>1</sup>, Dan J.L. Brett<sup>2</sup>, Paul R. Shearing<sup>2,\*</sup>, Jusef Hassoun<sup>1,3,\*</sup>

<sup>1</sup> *University of Ferrara, Department of Chemical and Pharmaceutical Sciences, Via Fossato di Mortara 17, 44121, Ferrara, Italy.*

<sup>2</sup> *Electrochemical Innovation Lab, Department of Chemical Engineering, UCL, London, WC1E 7JE, United Kingdom*

<sup>3</sup> *National Interuniversity Consortium of Materials Science and Technology (INSTM) University of Ferrara Research Unit, University of Ferrara, Via Fossato di Mortara, 17, 44121, Ferrara, Italy.*

Corresponding Authors: [jusef.hassoun@unife.it](mailto:jusef.hassoun@unife.it), [p.shearing@ucl.ac.uk](mailto:p.shearing@ucl.ac.uk).

† Authors equally contributed

## Abstract

Herein we originally depict the process of a novel sulfur nanocomposite by combining X-ray computed tomography at micro- and nanoscale and electrochemistry in lithium cell. The electrode is obtained at mild temperature according to an alternative approach including metal nanoparticles of either tin or nickel in a bulk of melted sulfur in the weight ratio of 85:15, respectively. We show that this pathway leads to highly performing electrodes, matching the state-of-the-art results on the best carbonaceous composites. Indeed, lithium-sulfur cells with a working voltage of about 2.2 V ensure a capacity referred to the sulfur mass approaching 1400 mAh g<sup>-1</sup> at a C/3 rate and 740 mAh g<sup>-1</sup> at a rate as high as 3C (1C = 1675 mAh g<sup>-1</sup>), with coulombic efficiency close to 100% and stable cycling trend over 100 cycle. High-resolution imaging sheds light on characteristic morphological features of the electrode that allow these remarkable performances, and reveals the beneficial effect of an actual metal nanoparticle incorporation within the sulfur phase. The various investigation techniques, with particular focus on three-dimensional imaging, suggest a sulfur electrodeposition upon charge preferentially next to electron conductive centers within the electrode support as well as on the metal

clusters. A massive microstructural reorganization is observed during the first cycle in lithium cell with concomitant remarkable enhancement of the electrode charge transfer and variation of the reaction potentials. This process is accompanied by a substantial electrode amorphization and migration of the active material towards the current collector bulk. The results obtained in this work, and a comprehensive study designed *ad hoc* for the sulfur electrode, suggest alternative strategies for ultimately achieving an actual Li/S cell improvement.

## Introduction

Lithium-ion batteries are currently based on intercalation electrodes<sup>1</sup> allowing long cycle life, high efficiency,<sup>2</sup> and an energy density up to about 260 Wh kg<sup>-1</sup>.<sup>3</sup> A great deal of research over the past three decades has triggered their large-scale diffusion and application in advanced portable electronics, such as laptops and smartphones, in hybrid and full electric vehicles (HEV and EV, respectively), as well as in high-capacity stationary storage facilities.<sup>4-7</sup> In spite of the rapid growth of the lithium-ion battery in the market promoted by environmental policies aimed at decarbonization of road transport and exploitation of renewable sources in several countries,<sup>7</sup> part of the scientific community is now focusing on alternative chemistries, *i.e.*, beyond lithium-ion systems, to boost the energy performance at the cell level.<sup>8</sup> Among the proposed alternatives, the lithium-sulfur battery is an almost mature technology<sup>9</sup> based on the multi-electron conversion of environmentally-friendly, inexpensive sulfur to lithium sulfide (Li<sub>2</sub>S), that is,  $S_8 + 16Li^+ + 16e^- \rightleftharpoons 8Li_2S$ ,<sup>10,11</sup> leading to a theoretical energy density as high as 2600 Wh kg<sup>-1</sup> referred to the Li<sub>2</sub>S mass.<sup>12</sup> Sulfur conversion process occurs through multiple steps involving lithium polysulfide intermediates, *i.e.*, Li<sub>2</sub>S<sub>x</sub> where  $2 \leq x \leq 8$ , which are soluble in the conventional electrolyte media for  $x \geq 4$ .<sup>8,10</sup> Hence, long-chain polysulfides may migrate to the anode and directly react with lithium metal, thus leading to active material loss, capacity fading, and poor coulombic efficiency which is further decreased by a process indicated as “*shuttle effect*” consisting of apparent charge without any energy storage due to concomitant oxidation of polysulfide at the cathode and migration with direct reduction at the

anode.<sup>11,13</sup> Suitable ether-based electrolytes upgraded by the inclusion of lithium nitrate ( $\text{LiNO}_3$ ) as a sacrificial film forming agent have effectively mitigated the shuttle effect by preventing direct reaction of the protected lithium metal with the dissolved polysulfides.<sup>14</sup> On the other hand, significant efforts have been devoted to optimizing composite cathodes formed by conductive carbon matrixes confining sulfur in order to prevent the lithium polysulfide dissolution and enhance the electron transport, thus improving the electrode performances.<sup>15</sup> Accordingly, inert carbon structures obtained *via* advanced synthetic strategies, such as nanotubes,<sup>16,17</sup> 3D-array graphene,<sup>18</sup> hierarchical porous carbon<sup>19</sup> and nanospherules,<sup>20</sup> may provide adequate electric contact for the insulating S,  $\text{Li}_2\text{S}$ , and  $\text{Li}_2\text{S}_2$  particles<sup>21</sup> and efficiently trap the soluble intermediates for decreasing the shuttle magnitude.<sup>15</sup> Furthermore, the functionalization of carbon materials with heteroatoms potentially able to chemically interact with  $\text{Li}_2\text{S}_x$  species ( $x \geq 4$ ), such as N and P, has been widely explored as an effectual way to limit the polysulfide shuttle and improve the electrochemical reaction.<sup>22,23</sup> Recently, composite carbon structures including transition-metal compounds have revealed favorable coordination properties for limiting polysulfides mobility within the Li/S cell.<sup>24-27</sup>

However, relatively high fractions of inert carbon matrices used for ensuring satisfactory electron conductivity actually affects both the gravimetric and the volumetric energy densities of the composite.<sup>28</sup> Therefore, we have lately proposed a *new-concept* electrode consisting of a sulfur bulk loaded by nanometric tin particles for achieving high-performances and, at the same time, a relevant content of the active material. The related paper reports a proof-of-concept study on the structure, morphology, composition of a novel S:Sn composite (80:20 by weight, respectively) which has shown promising cell behavior.<sup>29</sup> It is worth mentioning that the beneficial effect of conductive metal nanoparticles has been previously demonstrated using various electrodes studied for lithium-ion battery application.<sup>30-32</sup> Interestingly, our encouraging preliminary data on the sulfur-tin nanocomposite supported on a carbon-cloth current collector have indicated this alternative approach as well-suited for sulfur cathodes too.<sup>29</sup> Furthermore, sulfur-metal electrodes might possibly benefit from a higher expected tap density compared to composite materials using porous carbon

matrices<sup>19,28,33,34</sup> as well as by a simple preparation pathway.<sup>29</sup> Hence, a thorough investigation of sulfur-metal composites may be of actual importance to shed light on the effect of nanoparticles on the multiphase sulfur conversion process in lithium cell.

Accordingly, we aim to provide herein a comprehensive description of the electrochemical reorganization occurring in the positive electrode through various experimental techniques. New electrode formulations including either tin or nickel nanometric powders and increasing the sulfur weight ratio to a value as high as 85% are considered. We thoroughly describe the materials, their electrochemical evolution in the cell and the reaction kinetics through an interdisciplinary approach combining various experimental techniques, namely X-ray computed tomography at the micro- and nanoscale, X-ray diffraction, electron microscopies, energy dispersive X-ray spectroscopy, voltammetry, and impedance spectroscopy. In particular, high-resolution tomographic datasets may elucidate the remarkable microstructural reorganization occurring upon reversible sulfur conversion in the battery, by enabling a three-dimensional reconstruction of the electrode,<sup>35</sup> while in-depth diffraction, microscopy and electrochemical analyses may shed light on the evolution of crystal structure, morphology, reaction potentials and electrode kinetics. Hence, an outstanding electrochemical behavior is demonstrated by cycling tests within current rates ranging from C/3 to 3C, while the intrinsic effects of the two metals is revealed to control the electrode/electrolyte interphase and the rate capability up to values as high as 10C. The novel findings and electrode formulations as well as the alternative approach adopted in this study may actually be of definite importance for achieving high-performance Li/S battery.

## **Experimental**

Nanocomposites were prepared by physically mixing elemental sulfur (Sigma-Aldrich) with either tin (<150 nm, Sigma-Aldrich,  $\geq 99\%$  trace metal basis) or nickel (<100 nm, Sigma-Aldrich,  $\geq 99\%$  trace metal basis) powders in a weight ratio of 85:15. The mixtures were heated in a silicon oil bath at 120 °C under magnetic stirring until complete melting of sulfur and subsequently quenched at room

temperature until sulfur solidification. The materials so obtained were grinded in an agate mortar to get fine powders, which are indicated as S:Sn 85:15 w/w and S:Ni 85:15 w/w in the manuscript.

Crystal structure of the nanocomposites was studied by X-ray diffraction (XRD) through a Bruker D8 Advance diffractometer equipped with a Cu-K $\alpha$  source by performing a scan in the 2 $\theta$  range between 10° and 90° at a rate of 10 s step<sup>-1</sup> with a step size of 0.02°. Powder morphology was investigated by scanning and transmission electron microscopies (SEM and TEM, respectively) through a Zeiss EVO 40 microscope with a LaB<sub>6</sub> thermionic electron gun and through a Zeiss EM 910 microscope with a tungsten thermionic electron gun operating at 100 kV, respectively. The elemental distribution in the composites was determined by collecting energy dispersive X-ray spectroscopy (EDX) maps through the X-ACT Cambridge Instruments analyzer of the SEM equipment. Selected area electron diffraction (SAED) was carried out by the above-mentioned TEM microscope.

The S:Sn 85:15 w/w and S:Ni 85:15 w/w powders were investigated by X-ray nano-computed tomography (CT) through a Zeiss Xradia 810 Ultra instrument (Carl Zeiss Inc.) equipped with a micro-focus rotating Cr anode with characteristic energy at 5.4 keV (Cr-K $\alpha$ , MicroMax-007HF, Rigaku) set at 35 kV and 25 mA. The instrument had a capillary condenser located in a He-filled chamber concentrating the quasi-monochromatic, quasi-parallel X-ray beam on the sample, a pinhole blocking unwanted scattered X-rays from the sample stage, and a zone plate in a He-filled optics chamber that focuses the X-ray beam on a CCD detector. Nano-CT scans were carried out in X-ray absorption-contrast, large-field-of-view (65  $\mu$ m) mode with 1 voxel binning, by taking 1601 projections through 180° with exposure time of 46 and 55 s for S:Sn 85:15 w/w and S:Ni 85:15 w/w, respectively, thereby leading to a voxel size of about 63 nm. Samples for nano-CT were prepared by attaching a small amount of powder on stainless steel (SS) needles by an epoxy glue [2,4,6-tris(dimethylaminomethyl)phenol, Devcon] with the support of an optical microscope. The tomographic datasets were reconstructed by the Zeiss XMReconstructor software (Carl Zeiss Inc.) employing a filtered back-projection algorithm. The nano-CT data were processed by applying non-

local means and unsharp masking filters, segmented, and imaged through Avizo 2019.2 (Visualization Sciences Group, FEI Company). Three domains with increasing X-ray attenuation were identified by employing a grayscale threshold method:<sup>36,37</sup> (i) exterior, (ii) sulfur, (iii) metal nanoparticles.

Two composite electrodes were made by mixing the S:Sn 85:15 w/w or S:Ni 85:15 w/w powders (80 wt.%), respectively, Super P carbon as conducting agent (10 wt.%, Timcal) and polyvinilidene fluoride as binder (10 wt.%, PVDF 6020, Solef Solvay). The components were dispersed in N-methyl-2-pyrrolidone (NMP, Sigma-Aldrich) to obtain a uniform slurry that was cast on a carbon-cloth foil (ELAT 1400, MTI Corp.) by means of a doctor blade. The carbon-cloth foil had a thickness of 454  $\mu\text{m}$ , a density of 0.8  $\text{g cm}^{-3}$ , a carbon content of 95.5% in woven, and a rough surface suitable for hosting sulfur (see the related SEM images collected through a Zeiss EVO MA10 equipped with a tungsten thermionic electron gun in Figure S1 of the Electronic Supplementary Information). The cast slurries were heated at 50  $^{\circ}\text{C}$  for about 3 hours to remove the solvent and subsequently cut into 14 mm diameter disks by using a punch. The electrode disks were dried at 45  $^{\circ}\text{C}$  under vacuum overnight to eliminate residual solvent and water traces, and then stored in an Ar-filled glovebox (MBraun,  $\text{O}_2$  and  $\text{H}_2\text{O}$  content below 1 ppm). Two electrode batches with sulfur loading of about 2  $\text{mg cm}^{-2}$  and within 6 and 7  $\text{mg cm}^{-2}$ , respectively, were prepared for each sulfur-metal nanocomposite by properly adjusting coating thickness (about 500 and 700  $\mu\text{m}$ , respectively) and quantity of solvent. Further electrodes on a Cu current collector foil (thickness of 25  $\mu\text{m}$ , MTI Corp.) were prepared through the above reported procedure. The current Cu collectors were analyzed by XRD through a Bruker D8 Advance diffractometer equipped with a Cu-K $\alpha$  source by performing a scan in the  $2\theta$  range between 20 $^{\circ}$  and 90 $^{\circ}$  at a rate of 10  $\text{s step}^{-1}$  with a step size of 0.02 $^{\circ}$ .

CR2032 coin-cells (MTI Corp. and Hohsen Corp.) were assembled in an Ar-filled glovebox (MBraun,  $\text{O}_2$  and  $\text{H}_2\text{O}$  content below 1 ppm) by stacking a composite electrode, a Celgard 2400 separator soaked by either 50  $\mu\text{l}$  (for sulfur loading of about 2  $\text{mg cm}^{-2}$ ) or 80  $\mu\text{l}$  (for sulfur loading within 6 and 7  $\text{mg cm}^{-2}$ ) of electrolyte solution, and a lithium disk with a diameter of 14 mm. Cells

for *ex situ* characterization were prepared by employing a moderately lower pressure than usual in order to facilitate disassembling after tests. The electrolyte solution was prepared by dissolving lithium bis(trifluoromethanesulfonyl)imide (LiTFSI) and lithium nitrate (LiNO<sub>3</sub>) in a mixture of 1,3-dioxolane (DOL) and 1,2-dimethoxyethane (DME) in the 1:1 weight ratio. The final salt concentration with respect to the solvent mass was 1 mol kg<sup>-1</sup> for LiTFSI and either 1 or 0.4 mol kg<sup>-1</sup> for LiNO<sub>3</sub>. The DOL:DME 1:1 w/w, 1 mol kg<sup>-1</sup> LiTFSI, 1 mol kg<sup>-1</sup> LiNO<sub>3</sub> composition was used for all the electrochemical measurements, while the DOL:DME 1:1 w/w, 1 mol kg<sup>-1</sup> LiTFSI, 0.4 mol kg<sup>-1</sup> LiNO<sub>3</sub> one was employed for the *ex situ* characterization.

The electrochemical behavior of the S:Sn 85:15 w/w and S:Ni 85:15 w/w electrodes in lithium cell was investigated by coupling cyclic voltammetry (CV) and electrochemical impedance spectroscopy (EIS). CV measurements were carried out within the 1.8 – 2.8 V vs Li<sup>+</sup>/Li range at a constant scan rate of 0.1 mV s<sup>-1</sup>. Impedance spectra were recorded upon voltammetry cycling, namely at the open circuit voltage (OCV) condition, after 1, 5 and 10 cycles, by applying to the cell an alternate voltage signal with an amplitude of 10 mV within the 500 kHz – 100 mHz frequency range. The impedance spectra were analyzed to evaluate the electrode/electrolyte interphase resistances through the Boukamp software according to a nonlinear least-square (NLLS) method.<sup>38</sup> The EIS response were modelled by the R<sub>e</sub>(R<sub>1</sub>Q<sub>1</sub>)(R<sub>2</sub>Q<sub>2</sub>)Q<sub>3</sub> equivalent circuit, where R<sub>e</sub> is attributed to the electrolyte resistance, the R<sub>i</sub>Q<sub>i</sub> (i = 1, 2) elements correspond to the electrode/electrolyte interphase resistances and pseudo-capacitances at high-middle frequency (including passivation films and charge transfer), and Q<sub>3</sub> represents low-frequency Li<sup>+</sup> diffusion processes.<sup>38-41</sup>  $\chi^2$  values of the order of 10<sup>-4</sup> – 10<sup>-5</sup> and low estimated errors on the resistances (see Tables 1 and 2) suggest the accuracy of the analyses.

CV at various scan rates, *i.e.*, 0.05, 0.1, 0.15, 0.2 and 0.25 mV s<sup>-1</sup>, within the 1.8 – 2.8 V vs Li<sup>+</sup>/Li range was carried to estimate the apparent Li<sup>+</sup> diffusion coefficient upon the electrochemical reaction according to the Randles-Sevcik equation (equation 1):<sup>42,43</sup>

$$I_p = 0.4463zFAC \left( \frac{zFvD}{RT} \right)^{1/2} \quad (1)$$

where  $I_p$  is the peak current value (A),  $z$  is the number of exchanged electrons,  $F$  is the Faraday constant (96485 C mol<sup>-1</sup>),  $A$  is the geometric area of the electrodes (cm<sup>2</sup>),  $C$  is the estimated volumetric concentration of Li<sup>+</sup> in the electrode volume (mol cm<sup>-3</sup>),  $v$  is the scan rate (V s<sup>-1</sup>),  $D$  is the diffusion coefficient (cm<sup>2</sup> s<sup>-1</sup>),  $R$  is the gas constant (8.31451 J mol<sup>-1</sup> K<sup>-1</sup>) and  $T$  is the temperature (298 K). The CV and EIS measurements were performed by a VersaSTAT MC Princeton Applied Research (PAR) analyzer.

The electrochemical performances of the S:Sn 85:15 w/w and S:Ni 85:15 w/w nanocomposites in lithium cell were assessed by galvanostatic cycling at various current rates ( $C/x$ ), considering a 1C rate of 1675 mA g<sup>-1</sup> as referred to the sulfur mass in the electrode. These measurements were performed through a MACCOR series 4000 battery test system. Li | DOL:DME 1:1 w/w, 1 mol kg<sup>-1</sup> LiTFSI, 1 mol kg<sup>-1</sup> LiNO<sub>3</sub> | cathode cells with a sulfur loading of about 2 mg cm<sup>-2</sup> were tested at constant rates of C/3, 1C, 2C and 3C over 100 cycles, by adjusting the voltage range to 1.9 – 2.8 V for the C/3 and 1C rates, and to 1.8 – 2.8 V for the 2C and 3C rates. Li | DOL:DME 1:1 w/w, 1 mol kg<sup>-1</sup> LiTFSI, 1 mol kg<sup>-1</sup> LiNO<sub>3</sub> | cathode cells with a high sulfur loading (6.8 and 6.3 mg cm<sup>-2</sup> for S:Sn 85:15 w/w and S:Ni 85:15 w/w, respectively) were cycled at a constant current rate of C/20 within the voltage range of 1.9 – 2.8 V. Two rate capability tests for each Li | DOL:DME 1:1 w/w, 1 mol kg<sup>-1</sup> LiTFSI, 1 mol kg<sup>-1</sup> LiNO<sub>3</sub> | cathode cell (sulfur loading of about 2 mg cm<sup>-2</sup>) were carried out by increasing the current rate every 5 cycles from C/10 to 2C and from 1C to 10 C, respectively, and decreasing the current to the initial values after 35 cycles. In detail, the cells were tested at C/10, C/8, C/5, C/3, C/2, 1C, 2C, 3C, 4C, 5C, 8C, and 10C rates within the voltage ranges of 1.9 – 2.8 V (from C/10 to C/2) and 1.8 – 2.8 V (from 1C to 10C). Galvanostatic cycling tests of the S:Sn 85:15 w/w and S:Ni 85:15 w/w cathodes over about 300 cycles were carried out on Li | diethylene glycol dimethyl ether (DEGDME, 99.5%, Sigma-Aldrich), 1 mol kg<sup>-1</sup> LiTFSI, 1 mol kg<sup>-1</sup> LiNO<sub>3</sub> | cathode cells with sulfur loading of about 2 mg cm<sup>-2</sup>. The cells were cycled at a 1C rate

within the voltage range of 1.8 – 2.8 V. The electrodes cast on Cu were galvanostatically cycled at a C/3 rate within the voltage range of 1.9 – 2.8 V.

The S:Sn 85:15 w/w and S:Ni 85:15 w/w electrodes were investigated before and after cycling by combining XRD, SEM, SEM-EDX, and X-ray micro-CT measurements. The electrodes were galvanostatically cycled in Li | DOL:DME 1:1 w/w, 1 mol kg<sup>-1</sup> LiTFSI, 0.4 mol kg<sup>-1</sup> LiNO<sub>3</sub> | cathode cells at a C/3 rate (where 1C = 1675 mA g<sup>-1</sup>, referred to the sulfur mass) within a voltage range of 1.9 – 2.8 V through a MACCOR Model 4300 battery test system. The cells were disassembled in an Ar-filled glovebox (MBraun, O<sub>2</sub> and H<sub>2</sub>O content below 1 ppm); the cathodes were recovered and dried under vacuum for 30 minutes in the glovebox antechamber. The electrode samples were exposed to the atmosphere upon the XRD, SEM, SEM-EDX, and micro-CT measurements. The XRD patterns were collected through a Rigaku SmartLab instrument equipped with a Cu-K $\alpha$  source by performing a scan in the 2 $\theta$  range between 10° and 90° at a rate of 0.4° min<sup>-1</sup> with step size of 0.01°. SEM and SEM-EDX images were collected by means of a Zeiss EVO MA10 equipped with a tungsten thermionic electron gun and a INCA X-ACT Oxford Instrument analyzer.

X-ray micro-CT datasets were obtained through a Zeiss Xradia 520 Versa instrument (Carl Zeiss Inc.) employing a polychromatic micro-focus source (tungsten target) set at 80 kV and 88  $\mu$ A. Samples for micro-CT were prepared by cutting out a disk with diameter of 1 mm from each electrode, and attaching the disk to a SS dowel by an epoxy glue [2,4,6-tris(dimethylaminomethyl)phenol, Devcon]. Source and detector distances from the sample stage and X-ray exposure time were adjusted in order to get suitable transmission values. Tomographic datasets were collected by using 20X objective lens and taking 1601 projections through 360° with an exposure time from 22 to 40 s and 1 voxel binning. The experimental conditions led to a voxel size from 288 to 373 nm, and a field of view from about 570 to about 730  $\mu$ m. The tomographic datasets were reconstructed by the Scout-and-Scan Control System Reconstructor software (Carl Zeiss Inc.) employing a filtered back-projection algorithm. The micro-CT data were processed by applying non-local means and unsharp masking filters, segmented, imaged, and analyzed through Avizo 2019.2 (Visualization Sciences

Group, FEI Company). The adopted voxel size allowed us the identification of five domains with increasing X-ray attenuation by employing a grayscale threshold method:<sup>36,37</sup> (i) exterior, (ii) carbon/binder/carbon-cloth, (iii) isolated sulfur, (iv) sulfur-metal nanoparticle intimate mixture, (v) isolated metal domain. Binary datasets were produced after segmentation to evaluate the particle size distribution of the domain formed by isolated sulfur and intimate mixture of sulfur and metallic nanoparticles. In detail, the sulfur and sulfur-metal nanoparticle intimate mixture domains (iv and v) were merged in a single segmentation phase, which was processed by particle separation tools through Avizo 2019.2 (Visualization Sciences Group, FEI Company) and analyzed through the ImageJ plugin XLib.<sup>44</sup> The sphericity (shape factor) of the particles was calculated according to equation 2:

$$(\textit{Sphericity}) = \pi^{1/3} \frac{(6V)^{2/3}}{A} \quad (2)$$

where V and A are the estimated volume and surface of the particles.

All the measurements were carried out at 25 °C.

## Results and discussion

Microstructural characteristics of the sulfur-metal nanocomposites are revealed in Figure 1, and in Figures S2 and S3 in the Electronic Supplementary Information, by combining of X-ray diffraction, nano-CT, electron microscopy, as well as EDX. The XRD patterns in Figure S2 show the structural features of elemental sulfur and metal nanoparticles in both samples, thus suggesting absence of impurities formed by parasitic reactions during the synthesis,<sup>45,46</sup> such as metal sulfides, which might affect the electrochemical process in lithium cell.<sup>47</sup> These results suggest the mild-temperature mixing of sulfur and metallic nanopowders as suitable approach for achieving pure nanocomposite materials possibly benefiting from the dispersion of electronically-conductive, crystalline tin and nickel particles within a sulfur matrix.<sup>31,48</sup> Figure 1 shows the nanocomposite morphology detected by SEM-EDX, TEM and X-ray nano-CT for S:Sn 85:15 w/w and S:Ni 85:15 w/w. The former sample is mostly composed of nanometric tin particles ( $\leq 200$  nm, see the secondary-electron image of panel a inset) which form micrometric agglomerates ranging from 5 to 40  $\mu\text{m}$ , visible as bright domains in the

backscattering image of panel a as well as in the EXD maps of panel c. Metallic tin is surrounded by a sulfur phase, observed both in panel a as a dark-gray matrix and in the EDX image of panel b. As for the latter sample, the secondary-electron image of panel d inset suggests Ni primary particles ranging from about 100 nm to about 1  $\mu$ , which are arranged into secondary structures ranging from 50 to 100  $\mu$ m beside micrometric sulfur, as shown by the backscattering and EDX images in panels d, e and f, respectively. Furthermore, panels g-n reveal a rather different morphology of the sulfur-metal agglomerates at the nanoscale, suggesting a more intimate mixing between the two phases for S:Sn 85:15 w/w with respect to S:Ni 85:15 w/w. TEM and X-ray nano-CT may provide qualitative information on the sample composition as the density of the various phases forming the composite are directly reflected into the attenuation coefficient for the incident beam.<sup>37</sup> Accordingly, the relevant difference of sulfur and metal densities (2.07, 7.31 and 8.9 g/cm<sup>3</sup> at 25 °C for S, Sn and Ni, respectively)<sup>49</sup> allows unambiguous phase identification: metal particles/agglomerates are therefore observed in the TEM images (Figure 1g, k) and X-ray nano-CT reconstructions (Figure 1h, l and Figure S3 in the Electronic Supplementary Information) as highly attenuating domains (dark and bright particles, respectively), while sulfur exhibits relatively low attenuation (gray phase in both TEM and X-ray nano-CT images). Interestingly, electron microscopy and X-ray tomography fully agree in displaying S:Sn 85:15 w/w as tin particles and aggregates embedded into a sulfur matrix (compare Figure 1g and S3a in the Electronic Supplementary Information), which is a promising morphological feature for allowing suitable electrode performance particularly at high current rates.<sup>29</sup> On the other hand, S:Ni 85:15 w/w is formed by bigger, segregated metallic clusters beside micrometric sulfur particles (see Figure 1k and S3b in the Electronic Supplementary Information), thereby suggesting a possible lower rate capability mostly due to increased average electron paths.<sup>48</sup> The nano-CT datasets have been segmented based on the X-ray attenuation by using a grayscale threshold method,<sup>36,37</sup> as shown in the slices of panels h-i and l-m in Figure 1, where exterior, sulfur, tin and nickel are depicted in black, yellow, blue and green, respectively. Hence, segmented volume renderings of a single sulfur-metal agglomerate in panels j and n with the related insets reporting only

the metal domains clearly show that tin is mostly embedded within the sulfur phase, while nickel is hosted on the surface. Moreover, SAED insets of panels g and k confirm the crystalline nature of the metals in agreement with XRD.<sup>50,51</sup> Hence, the in-depth material characterization above discussed by means of XRD, electron microscopy and X-ray nano-CT advantageously reveals a detailed sketch of the composite microstructure, which is expected to strongly affect the electrode behavior in lithium cell according to the complex Li-S conversion mechanism.<sup>8</sup>

### Figure 1

Voltammetry and electrochemical impedance spectroscopy upon discharge/charge cycles are employed to detect the reaction potentials and electrode kinetics in a lithium-sulfur cell using a typical ether-based electrolyte consisting of LiTFSI and LiNO<sub>3</sub> salts dissolved in DOL/DME mixture. Figure 2 which reports the voltammograms performed at a scan rate of 0.1 mV s<sup>-1</sup> of S:Sn 85:15 w/w (panel a) and S:Ni 85:15 w/w (panel b) evidences well-defined reduction and oxidation peaks as well as overlapping profiles over 10 cycles. The figure indicates reversible electrochemical processes characterized by remarkable stability, while a slightly different CV response during the first cathodic and anodic scans suggests electrode reorganizations promoted by the multiphase reaction mechanism along with formation of an adequate electrode/electrolyte interphases.<sup>35</sup> In detail, the first reduction is characterized by the presence of two peaks at about 2.25 and 2.00 V for S:Sn 85:15 w/w, and at 2.25 and 2.05 V for S:Ni 85:15 w/w, which have been attributed to gradual formation of long-chain and short-chain lithium polysulfides, *i.e.* Li<sub>2</sub>S<sub>x</sub> with  $x \geq 6$  and  $2 \leq x \leq 4$ , respectively, and possibly Li<sub>2</sub>S,<sup>52-55</sup> whereas the subsequent anodic scan reveals a broad double-peak between 2.30 and 2.45 V, corresponding to the oxidation of Li<sub>2</sub>S and lithium polysulfides with electrodeposition of Li metal at the anode and likely S<sub>8</sub> at the cathode.<sup>52,54</sup> The two electrodes exhibit moderate cell polarization suggesting low charge transfer resistance and fast kinetics of the electrochemical process.<sup>16,54</sup> A shift of the first cathodic peak to higher potential values during subsequent, that is, from 2.25 to 2.35 V, as well as a slight overvoltage decrease for the oxidation reactions further reflects the above mentioned electrode rearrangements. These phenomena have been already observed in

literature<sup>18,29,54,56</sup> along with an enhancement of the electrode kinetics by cycling which leads to an increase of sulfur utilization. In this regard, EIS measurements have shown a remarkable decrease of the electrode/electrolyte interphase resistance, suggesting favorable modifications of the cathode microstructure upon progressive lithiation of the active material<sup>18,29,56,57</sup> and perhaps minor irreversible reaction of the electrolyte species to form suitable electrode passivation layers.<sup>14</sup> In addition, the voltammograms of Figure 2a and b show a gradual slight decrease of the peak currents by cycling, which might be related to partial loss of the active material during the electrochemical process.<sup>8,53</sup> Impedance spectra performed upon CV, namely at the OCV and after 1, 5, and 10 cycles, confirm previous observations,<sup>18,29,56</sup> by revealing a massive drop of the electrode/electrolyte interphase resistance after the first cycle. Accordingly, the related Nyquist plots (Figure 2c and b for S:Sn 85:15 w/w and S:Ni 85:15 w/w, respectively) evidence a remarkable shrink of the overlapped high-middle frequency semicircles after the first cycle, which reflect overall resistance values falling from 26 and 138  $\Omega$  for S:Sn 85:15 w/w and S:Ni 85:15 w/w, respectively, to about 2  $\Omega$  (see the experimental section and Tables 1 and 2 for further details about the NLLS analysis).<sup>38</sup> It is worth noting that a higher initial electrode/electrolyte interphase resistance in S:Ni 85:15 w/w compared to S:Sn 85:15 w/w may be expected considering the better nanometric metal dispersion of the latter composite indicated by the analysis of Figure 1. The remarkable resistance decrease is in line with the beneficial electrode activation observed by CV, occurring upon electro-dissolution of elemental sulfur *via* formation of long-chain polysulfides, subsequent precipitation of  $\text{Li}_2\text{S}_x$  species ( $x \leq 2$ ),<sup>52-55</sup> and sulfur electrodeposition during charge, which gradually enhances  $\text{Li}^+$  and electron transfer at the cathode/electrolyte interphase.<sup>18,29,56</sup> In this scenario, previous studies have demonstrated a change of electrode morphology with respect to the pristine condition by cycling in lithium cell due to the growth of sulfur clusters during charge on preferred sites acting as nucleation points.<sup>35</sup>

CV measurement at various scan rates have been also carried out to calculate the apparent  $\text{Li}^+$  diffusion coefficient ( $D$ ) within the electrode according to equation 1 (Figure 2e and f; see the experimental section for further details).<sup>42,43</sup> Although the assumptions of the diffusion-limited model

proposed by Randles and Sevcik<sup>42,43</sup> might not describe in full the complex multistep and multiphase sulfur conversion mechanism, the method has been widely employed in literature to provide a suitable figure of merit for the electrode reaction rate.<sup>16,58–60</sup> Herein, the linear relation of the peak current ( $I_p$ ) and the square root of the scan rate ( $v^{1/2}$ , see Figure S4 in the Electronic Supplementary Information) actually suggests an electrochemical processes controlled by diffusion in agreement with equation 1. Therefore, we have calculated  $D$  by assigning one electron to each cathodic peak (at about 2.3 and 2.0 V, respectively) and two electrons to the broad anodic double-peak (at 2.4 V) based on the formal reaction in the cell, *i.e.*,  $S + 2Li^+ + e^- \rightleftharpoons Li_2S$  (Table S1 in the Electronic Supplementary Information shows the obtained  $D$  values). The plots of the apparent lithium diffusion coefficient as a function of the potential vs  $Li^+/Li$  reported in bottom panels of Figure 2e, f exhibit for both S:Sn 85:15 w/w and S:Ni 85:15 w/w  $D$  values ranging from  $10^{-8}$  to  $10^{-7}$   $cm^2 s^{-1}$ , which gradually decrease upon discharge and subsequent charge, thereby reflecting the already observed high-power capability of the sulfur conversion to long-chain polysulfides (mostly  $Li_2S_8$  and  $Li_2S_6$ , perhaps along with minor amount of  $Li_2S_4$ ).<sup>61</sup> The high apparent coefficients<sup>16,58–60</sup> observed by voltammetry possibly suggest a fast electrochemical process benefiting from the metal particles, which ensure low electrode/electrolyte interphase resistance and high reversibility.

### Figure 2

The aforementioned material reorganizations, occurring upon cycling and accounting for the electrochemical behavior observed in Figure 2, is actually investigated in Figure 3 by *ex situ* XRD, SEM-EDX, and X-ray micro-CT measurements performed on the S:Sn 85:15 w/w and S:Ni 85:15 w/w electrodes before and after cycling in lithium cells (see the experimental section for further details). Panels a and b of Figure 3 show the XRD patterns of the S:Sn 85:15 w/w and S:Ni 85:15 w/w electrodes, respectively, in pristine condition and after 1 and 10 galvanostatic cycles at a  $C/3$  rate ( $1C = 1675$   $mA\ gs^{-1}$ ; see the related voltage profiles in Figure S5 of the Electronic Supplementary Information). The patterns of pristine samples exhibit the expected reflections of orthorhombic sulfur ( $\alpha$ - $S_8$ , ICSD # 27840) and metals (where the tin and nickel references are ICSD # 40038 and ICSD #

672759, respectively) in full agreement with the already discussed XRD data on the related powders (Figure S2 in the Electronic Supplementary Information), along with a broad peak centered at about  $26^\circ$  ( $2\theta$ ) due to the carbon-cloth support.<sup>62</sup> Notably, XRD after 1 and 10 cycles indicates a substantial decrease in crystallinity for the sulfur phase, while the diffraction peaks of metallic tin (panel a) and nickel (panel b) are clearly not affected by the electrochemical process. Hence, the sulfur peaks of S:Sn 85:15 w/w are relevantly broader and less intense after 1 cycle than in pristine conditions (panel a), thereby suggesting either an incomplete conversion during charge or perhaps a deposition of amorphous, rather than crystalline, sulfur.<sup>63,64</sup> Such a crystallinity loss is even more evident in the patterns of S:Ni 85:15 w/w (panel b). The patterns after 10 cycles evidence further minor reorganizations, namely a slight change of the relative peak intensities within the sulfur phase in S:Sn 85:15 w/w, which might be ascribed to possible deposition of crystalline long-chain polysulfides after electrode drying (see the experimental section for further details about the cell disassembly),<sup>29</sup> as well as a minor decrease in crystallinity for both electrodes.

Figure S6 in the Electronic Supplementary Information reports SEM-EDX images of the electrodes before and after 1 and 10 cycles. The pristine samples (panels a-f for S:Sn 85:15 w/w and panels g-l for S:Ni 85:15 w/w) are characterized by a rather uniform distribution of large micrometric sulfur particles and metal agglomerates, while more apparent segregation is observed for S:Ni 85:15 w/w, thus in agreement with the results of Figure 1. Furthermore, the samples reveal homogeneous dispersion of C and F attributed to the conductive agent and PVDF binder used for electrode preparation. Secondary-electron SEM images detected with higher magnification (panels f and l) confirm the same morphological features of Figure 1 for the Sn and Ni particles. The micrographs of Figure S6 reveal a huge morphological changes after 1 cycle (panels m-r for S:Sn 85:15 w/w and panels s-x for S:Ni 85:15 w/w), mainly consisting in a decrease of the sulfur particle size and deposition of oxygen-containing species at the surface which are reasonably attributed both to the electrolyte and to possible thin passivation layers. The analysis indicates the formation of large, irregular sulfur particles approaching  $80\ \mu\text{m}$  which are less intimately mixed with the other electrode

components in S:Sn 85:15 w/w, while few small sulfur particles (from about 30 to about 70  $\mu\text{m}$ ) are detected in S:Ni 85:15 w/w. Besides the micrometric sulfur particles, EDX reveals a homogenous dispersion of elemental S over the samples suggesting possible presence of lithiated sulfide species over the electrode as well as submicrometric sulfur domains. The images after 10 cycles (panels y-di for S:Sn 85:15 w/w and panels ei-ji for S:Ni 85:15 w/w) show a further decrease of the average sulfur particle size which is in full agreement with the low crystallinity evidenced by XRD (see Figure 3a and b), while the other electrode components appear unaltered by the ongoing of the cycles.

Although SEM-EDX effectively proves significant morphological changes occurring during the first cycle by detecting the elemental distribution over the electrode surface, X-ray CT may provide further insight on the spatial rearrangement of the various components within the bulk by three-dimensional imaging. Previous works have investigated the Li/S process by tomography in order to reveal the morphological evolution and the related degradation phenomena occurring in the cell.<sup>35,65–67</sup> However, these papers have mostly focused on the fundamental characterization of the electrochemical reactions in *ad hoc* cell geometries using small samples of composite S-C electrodes and having a very short cycle life (a few cycles). On the other hand, we aim to provide herein a comprehensive description of the cathode microstructural reorganizations in highly performing coin-cells. Thus, panels c, e, g, and i of Figure 3 report a volume rendering of the micro-CT datasets for S:Sn 85:15 w/w (c, g) and S:Ni 85:15 w/w (e, i) performed by using a grayscale representation which reflects the X-ray attenuation within the sample. Metallic clusters are clearly visible in the pristine electrodes (panels c and e) as bright domains (highly attenuating phase) laying on the carbon-cloth surface (lowly attenuating phase) together with gray larger sulfur particles (moderately attenuating phase) and a lowly attenuating carbon/binder mixture. Further domain with moderately-high attenuation coefficient is detected in the S:Sn 85:15 w/w sample (panel c) and attributed to the intimate mixture between S and Sn particles according to Figure 1. In this regard, it is noteworthy that the relatively high voxel size of the micro-CT datasets (of the order of 300 nm) avoids clear discerning of smaller S-metal agglomerates, which therefore appear as a continuous single phase.

Interestingly, the absence of the moderately-high attenuating domain in S:Ni 85:15 w/w suggests partial segregation of the metal clusters in agreement with Figure 1. Panels d and f of Figure 3 illustrate the segmentation based on the grayscale thresholding<sup>36,37</sup> of cross-sectional slices extracted in a plane orthogonal to the pristine electrode surface. Therefore, according to X-ray tomography the electrodes are formed by a dense mixture of metallic clusters and sulfur deposited over a light, highly porous carbon-cloth current collector. In addition, the data confirm the different microstructure of the S-metal agglomerates in S:Sn 85:15 w/w and S:Ni 85:15 w/w, as already suggested by TEM and nano-CT, and reveal a more intimate mixture for the former nanocomposite.

The X-ray imaging of panels g-j evidences that S:Sn 85:15 w/w (Figure 3 g-h) and S:Ni 85:15 w/w (Figure 3 i-j) electrodes undergo comparable microstructural reorganizations upon the first cycle, which lead to electrodeposition of sulfur particles within the porosity of the carbon-cloth as well as next to the metal clusters to form moderately-high attenuating domains, *i.e.*, S-Sn and S-Ni intimate mixtures. These observations match the *ex situ* SEM-EDX (Figure S6) showing a drop in the amount of sulfur located on the electrode surface by cycling, and with previous results on similar composite electrodes indicating sulfur migration within the carbon-based support during cycling.<sup>65</sup> Therefore, X-ray CT and SEM-EDX reveal that sulfur preferably deposit (*i*) close to the metal centers and (*ii*) within the current collector bulk (*i.e.*, not in proximity to the metals). Such a remarkable rearrangement may actually account for the electrochemical activation unequivocally observed in Figure 2. Apparently, sulfur electrodeposition easily occurs close to electron-conducting surfaces which suitably act as nucleation centers and possibly as chemisorption sites.<sup>68</sup> Therefore, it is reasonable to assume that newly electrodeposited sulfur has higher electric contact with the current collector than pristine sulfur,<sup>68</sup> thus accounting for the remarkable decrease of the electrode/electrolyte interphase resistance shown by EIS (Figure 2c and d).

### Figure 3

The X-ray micro-CT datasets have been further analyzed in Figure 4 and S7 of the Electronic Supplementary Information to evaluate the particle size distribution (PSD) of the sulfur domains

along with their sphericity (shape factor), also including the moderately-high attenuating phase formed by the intimate mixture of sulfur and metal clusters (light blue and light green for S:Sn 85:15 w/w and S:Ni 85:15 w/w, respectively). An overview of the particle distribution within the whole investigated field of view is given by Figure S7 which shows grayscale and segmented slices along the plane parallel to the electrode surface (panels a-b, e-f, i-j, and m-n) and the related volume renderings considering only sulfur and metal (panels c, g, k, and o). On the other hand, further segmented volume renderings in panels a, c, e, and g of Figure 4 display the migration of sulfur from the carbon-cloth surface in pristine condition (panels a and c for S:Sn 85:15 w/w and S:Ni 85:15 w/w, respectively) towards the support bulk after 1 cycle (panels e and g for S:Sn 85:15 w/w and S:Ni 85:15 w/w, respectively), along with the growth of the moderately-high attenuating domains, (light blue and light green, respectively) suggesting preferred sulfur electrodeposition next to Sn and Ni as well as within the carbon-cloth. A very interesting and detailed view of the electrode components is provided by animations showing the three-dimensional reconstructions and all the cross sectional slices orthogonal to the cathode surface (Movies S1, S2, S3, and S4 referred to pristine S:Sn 85:15 w/w, pristine S:Ni 85:15 w/w, S:Sn 85:15 w/w after 1 cycle, and S:Ni 85:15 w/w after 1 cycle, respectively). The related PSD analyses (Figure 4b, d, f, h) are obtained by processing the datasets of S and S-metal mixture domains in order to get discrete particles approximated to spheres with equivalent radius in the x-axes. The data reveal a decreasing trend from pristine to cycled electrode, thus in full agreement with the results of *ex situ* XRD and SEM-EDX. However, we would point out that the assumption of spherical particles represents a first approximation adopted herein to simplify the discussion since the actual shape of these particles may significantly differ, as indeed evidenced by both the imaging and the shape factor distribution of Figure S7. Panels b and d of Figure 4 suggest that about the 80% of analyzed phase in both S:Sn 85:15 w/w and S:Ni 85:15 w/w is distributed within particles of equivalent radii below 25  $\mu\text{m}$  (left y-axis), while the remaining volume fraction is composed of particles slightly larger than 30  $\mu\text{m}$  (right y-axis). A substantial reorganization leads to a particle size decrease after the first cycle (Figure 4f and h) according to radius values below 17 and

15  $\mu\text{m}$  for about the 80% of the phase volume of S:Sn 85:15 w/w and S:Ni 85:15 w/w, respectively. Moreover, the shape factor distribution indicates electrodeposition of sulfur particles with lower sphericity compared to the pristine condition, which might reflect a gradual coalescence of neighbor sulfur domains. A comparable decrease in sphericity of the sulfur particles after the first discharge/charge cycle has been attributed in literature to possible formation of monoclinic sulfur ( $\beta\text{-S}_8$ ).<sup>35</sup>

#### Figure 4

Although X-ray CT cannot reveal the actual Li-S mechanism by detecting the various reaction intermediates, our multi-technique approach suggests an important role of Sn and Ni clusters in the sulfur nanocomposites as well as of the porous current collector for suitably enhancing the conversion reaction by steering the massive microstructural rearrangement within the electrode bulk during the electrochemical process. We have observed that the metal centers and the conductive C-cloth support may act as preferred S nucleation sites possibly improving the reaction kinetics. This important result is fully supported by the galvanostatic tests in lithium cells over 100 cycles at C/3, 1C, 2C and 3C rates ( $1\text{C} = 1675 \text{ mA gs}^{-1}$ ) reported in Figure 5 in terms of voltage profiles (panels a-b) and cycling trend (panels c-d). The data indicate an initial capacity increase promoted by the above mentioned particle reorganization with formation of suitable electrode/electrolyte interphases.<sup>14,18,29</sup> This trend is more relevant in cells using S:Ni 85:15 w/w (Figure 5b and d) rather than S:Sn 85:15 w/w (Figure 5b and d) as most likely due to the less uniform mixture between sulfur and Ni compared to Sn in pristine condition observed by XRD, SEM-EDX and X-ray CT. Thus, the cells deliver a high reversible capacity in the subsequent cycles through flat voltage profiles (Figure 4a-b) well overlapping to each other and reflecting the multiphase conversion signature observed by voltammetry in Figure 2. In detail, the two cells exhibit a comparable galvanostatic response characterized by two discharge plateaus at about 2.3 and 2.0 V reversed into two charge plateaus at about 2.2 and 2.4 V, and by a low polarization moderately increasing at high current rate. The cycling trends of S:Sn 85:15 w/w (Figure 5c) and S:Ni 85:15 w/w (Figure 5d) show maximum reversible

capacities of about 1000, 840, 820, 600 mAh gs<sup>-1</sup> and 1390, 960, 910, 740 mAh gs<sup>-1</sup> at C/3, 1C, 2C, 3C rates, respectively, coulombic efficiency approaching 100% along the whole test after the first cycle, and capacity retention after 100 cycles increasing from about 87% and 80% at the lowest rate to values exceeding 90% at the highest rate. These responses indicate highly performing electrode materials as well as efficient mitigation of the shuttle effect by the sacrificial LiNO<sub>3</sub> additive,<sup>8,9</sup> thereby demonstrating the suitability of the sulfur-metal composites herein obtained by an innovative approach advantageously replacing the conventional carbon-based additives with low relative amount of metal nanopowders, which possibly increases the material density while holding its improved performance.<sup>29</sup> Indeed, the decrease of metal fraction compared to previous preliminary study<sup>29</sup> actually enhances both gravimetric energy density and cycling behavior, while the detailed comparative investigation of the cathode microstructural reorganizations including different metals most importantly accounts for the cell response. Notably, according to the *ex situ* measurements the metal particles and the C-cloth current collector lead to a remarkable cell operation. In this regard, it is worth mentioning that carbon-containing woven supports may significantly improve the electrochemical performance.<sup>61</sup> In particular, a comparative study has revealed that a carbon-cloth support may ensure a higher reversible capacity and a lower polarization than conventional aluminum owing to enhanced charge transfer at electrode/electrolyte interphase.<sup>69</sup> The beneficial effect has been attributed to a better electric contact of the active material particles with the current collector as well as to a higher electrode wetting enabled by the relevant porosity and the favorable chemical nature of the carbon-cloth.<sup>69</sup> Moreover, the working voltage of S-based cathodes might suggest a possible suitability of copper-based current collectors, although previous works have revealed that sulfur-based composite slurries may form an unstable electrode film on Cu.<sup>70</sup> Several further tests on S:Sn 85:15 w/w and S:Ni 85:15 w/w electrodes cast on Cu foils (see the experimental section for further details of the casting procedure) confirm the literature results, suggesting possible formation of Cu<sub>2</sub>S during the coating process (see Figure S8a in the Electronic Supplementary Information). The related

electrodes exhibit a very poor electrochemical activity in lithium cell, as shown in Figure S8b and c of the Electronic Supplementary Information.

Although both the S:Sn 85:15 w/w and S:Ni 85:15 w/w nanocomposites demonstrate high performances in the optimized cell configuration herein adopted, the latter material exhibits higher capacity values, particularly at the relatively low rate of C/3, however with more pronounced fading by increasing the current. This behavior may be related to the sulfur-metal arrangements observed by XRD, SEM-EDX and X-ray CT as well as to different intrinsic characteristics of the tin and nickel clusters. Further investigation has been conducted to clarify this aspect by performing rate capability tests within a wide current range from C/10 to 10C rate ( $1C = 1675 \text{ mA gs}^{-1}$ ).

### Figure 5

Figure 6 reports the rate performances of S:Sn 85:15 w/w (panel a) and S:Ni 85:15 w/w (panel b) in terms of discharge capacity trend, while panels a and b of Figure S9 in the Electronic Supplementary Information show the related voltage profiles of steady-state cycles. The profiles of Figure S9 reveal the increase of polarization expected by raising the current and accompanied by a decrease of specific capacity. The S:Ni 85:15 w/w nanocomposite exhibits a higher capacity within the range from C/10 to 2C rate ( $1C = 1675 \text{ mA gs}^{-1}$ ) than the S:Sn 85:15 w/w one, namely about 1380, 1330, 1280, 1235, 1170, 1045 and 840  $\text{mAh gs}^{-1}$  at C/10, C/8, C/5, C/3, C/2, 1C and 2C *versus* 1020, 985, 950, 920, 900, 875 and 775  $\text{mAh gs}^{-1}$ , respectively (Figure 6a and b). On the other hand, the latter electrode has a higher rate capability, that is, a lower capacity decrease by raising the current, which well agrees both with the electrochemical results of Figure 5 and with the microstructural features detected by electron microscopy and X-ray tomography (Figures 1, 3, 4 and Figures S3, S6, S7 in the Electronic Supplementary Information). In addition, the S:Sn 85:15 w/w electrode fully recovers the initial capacity when the current is decreased to C/10 at the 36<sup>th</sup> cycle, while the S:Ni 85:15 w/w one shows a slight fading to 1240  $\text{mAh gs}^{-1}$ . Significant differences in rate performances of the electrodes are further evidenced by ranging the current from 1C to a value as high as 10C ( $1C = 1675 \text{ mA gs}^{-1}$ ). Indeed, S:Ni 85:15 w/w exhibits discharge capacities of 1130, 920, 820 and 690  $\text{mAh gs}^{-1}$  at 1C, 2C,

3C, and 4C, while S:Sn 85:15 w/w delivers 830, 725, 660 and 610 mAh gs<sup>-1</sup>, respectively. However, the first cycle at 4C of S:Ni 85:15 w/w (Figure 6b) is characterized by an abrupt drop of specific capacity to 320 mAh gs<sup>-1</sup> which is not observed in the case of S:Sn 85:15 w/w (Figure 6a). The better rate capability of the tin-based nanocomposite compared to the nickel-based one is clearly revealed by the cycling at 5C, 8C and 10C, which indicates capacity values of 560, 360 and 160 mAh gs<sup>-1</sup> for the former (Figure 6a), while 250, 160 and 120 mAh gs<sup>-1</sup> for the latter (Figure 6b). Importantly, both electrodes recover almost the initial capacity, *i.e.*, 795 mAh gs<sup>-1</sup> for S:Sn 85:15 w/w and 1095 mAh gs<sup>-1</sup> for S:Ni 85:15 w/w, as the current is decreased to 1C at the end of the test.

Our results evidence higher performances in terms of specific capacity for the nickel-based electrode, while higher rate capability for the tin-based one. However, both nanocomposites can be considered promising candidates for application in high-energy lithium-sulfur batteries based on state-of-the-art data.<sup>3,8,12,71</sup> Accordingly, the actual effect of the Sn and Ni additives may be evaluated by comparing our results with recent reports on carbonaceous composites in which we have used the same current collector (see the experimental section for further details). Sulfur was impregnated in a three-dimensional carbon framework in the weight ratio of 65%, thus leading to an active material loading over the electrode between 1.4 and 4.0 mg cm<sup>-2</sup>. The electrodes delivered a maximum capacity in lithium cells of ca. 1200 mAh gs<sup>-1</sup> at a C/10 rate, decreasing to values within 800 and 1000 mAh gs<sup>-1</sup> at a 1C rate, and exhibited a capacity retention from 70 to 80% after 100 cycles within the C/3 – 1C current range.<sup>18</sup> Nitrogen incorporation may enhance the reversibility of the conversion reaction in electrodes with a S loading within 2.0 and 2.8 mg cm<sup>-2</sup> (S:C 70:30 w/w), leading to a maximum capacity of about 1400 mAh gs<sup>-1</sup> at a C/10 rate and a capacity of about 1000 mAh gs<sup>-1</sup> from C/5 to C/2 rate with a retention higher than 95% after 100 cycles.<sup>57</sup> Other carbonaceous additives, such as multiwalled carbon nanotubes, may ensure a S:C ratio of 60:40 w/w, which is reflected into a composite electrode with a sulfur loading over the electrode from 3 to 4 mg cm<sup>-2</sup> delivering almost 1300 mAh gs<sup>-1</sup> at a C/8 rate, and exhibiting a stable capacity of 890 mAh gs<sup>-1</sup> for about 100 cycles at a 1C rate.<sup>16</sup>

It is worth considering that crucial parameters such as the electrode loading and thickness, the electrolyte/sulfur mass ratio (E/S), and the lithium-metal excess may significantly affect the actual energy density, leading to maximum practical values between 400 and 600 Wh kg<sup>-1</sup> with respect to the whole cell mass.<sup>12,72</sup> Therefore, we have attempted to further increase the active material loading aiming to match some of the expected requirements for commercial applications.<sup>72</sup> Panels c and d of Figure 6 show preliminary cycling results of S:Sn 85:15 w/w and S:Ni 85:15 w/w electrodes with loadings increased from the typical value used for material characterization (about 2/3 mgs cm<sup>-2</sup>) to 6.8 and 6.3 mgs cm<sup>-2</sup>, respectively, in lithium coin-cells using 80 μl of electrolyte solution (see the experimental section for further details about the cell assembly). The cells respectively deliver a capacity as high as 6.4 and 6.9 mAh cm<sup>-2</sup> referred to the electrode geometric area (1.54 cm<sup>2</sup>) at a C/20 rate (1C = 1675 mA gs<sup>-1</sup>), as shown by the top x-axis of the voltage profiles (Figure 6c and d) and by the right y-axis of the capacity trends (insets of panels c and d), which correspond to about 1000 and 1100 mAh gs<sup>-1</sup> (bottom x-axis of the voltage profiles and left y-axis of cycling trends). Such a relevant performance actually suggests the metal-nanocomposite approach as a viable strategy to achieve high-energy lithium-sulfur batteries, although additional work is certainly needed to match the strict demands of the battery market.<sup>72</sup> Further engineering of the electrode support, along with a careful optimization of the cell design, might fit the various figures of merit possibly promoting practical applications.<sup>12,72</sup> Based on our X-ray CT data, a large volume fraction of the carbon-cloth foil is not involved in the sulfur electrodeposition. Therefore, a much thinner carbon-cloth foil might reasonably increase the gravimetric energy density of the cell without compromising the performance. However, the technological optimization of the current collector, despite being of definite interest, is beyond the scope of our work.

Cycle life is considered to be a key parameter currently limiting an actual transition of the Li-S technology from laboratory to application.<sup>12</sup> Therefore, we have further demonstrated herein a stable electrode behavior over about 300 galvanostatic cycles at a 1C rate, that is, a current value close to practical requirements,<sup>72</sup> by employing a widely-investigated diglyme solution.<sup>16,57,73</sup> On the

other hand, The electrolyte formulation may alter the ionic conductivity and the lithium-ion transport within the electrolyte, as well as the passivation layer over the lithium metal anode.<sup>74</sup> Accordingly, DOL-DME-based electrolytes may decrease the cell polarization and enhance the rate capability of the cell, while diglyme-based solutions may mitigate the lithium dendrite formation at the anode side which is a suitable characteristic for allowing long-term cycling tests.<sup>16,18,57,73</sup> Furthermore, various cell components which have been optimized herein (such as sulfur-based composite, binder, current collector, electrolyte formulation, E/S ratio, and lithium anode) may affect the performance of such a complex system.<sup>9,69,75</sup>

Figure 6e and Figure S9c-d in the Electronic Supplementary Information show related cycling trend and voltage profiles, respectively. The cells reveal a remarkable response characterized by moderate polarization (Fig. S9c-d) and coulombic efficiency approaching 100% (Figure 6e). In particular, S:Sn 85:15 w/w exhibits lower specific capacity and higher retention than S:Ni 85:15 w/w which is in full agreement with the result of Figure 5, thereby suggesting a significant effect of chemical nature and morphology of the metal clusters on the cycling ability of the material. Relevantly, S:Sn 85:15 w/w and S:Ni 85:15 w/w deliver a maximum capacity of about 850 and 1030 mAh g<sub>S</sub><sup>-1</sup> with a retention after 300 cycles of about 72 and 70%. Previous works have shown that the use of Ni-based substrates for sulfur electrodes, such as foams and engineered porous foils, as well as sulfur composites including Ni fibers may enhance the electrochemical behavior of the cell due to possible beneficial effects on the polysulfide dissolution and the bulk electronic conductivity of the cathode.<sup>76-78</sup> However, state-of-the-art Ni-based electrodes delivered reversible capacities within the range from 400 to 800 mAh g<sub>S</sub><sup>-1</sup> for about 50 cycles at current rates from C/10 to C/2, with S loading between 0.9 and 2.0 mg cm<sup>-2</sup>.<sup>76-78</sup> In addition, we have lately demonstrated improved performances of a S:Sn 80:20 w/w composite, as mentioned above, that is, a capacity ranging from 1200 mAh g<sub>S</sub><sup>-1</sup> at C/10 to about 800 mAh g<sub>S</sub><sup>-1</sup> at 2C, with satisfactory cycling stability over 100 cycles and S loading between 1.2 and 2.0 mg cm<sup>-2</sup>.<sup>29</sup> Herein, we have further improved the electrochemical performances of the S-metal composites in terms of reversible capacity (maximum value approaching 1400 mAh

gs<sup>-1</sup>), rate capability (up to 560 mAh gs<sup>-1</sup> at 5C), cycle life (300 cycles with coulombic efficiency close to 100% and capacity retention of about 70%), and sulfur loading (up to 6.8 mg cm<sup>-2</sup>). Moreover, we have revealed in detail the electrode reorganizations possibly providing useful insight on the most effective strategies to enhance the Li-S cell. Such promising results indicate an alternative way to build highly performing Li-S cells matching the best literature results.<sup>9</sup>

### Figure 6

### Conclusions

New findings on the Li/S reaction have been revealed by *in-depth* study of nanocomposite electrodes prepared through an alternative approach by the inclusion of metallic clusters (tin and nickel), thus significantly differing from the widely investigated sulfur confinement in carbon hosts. The multi-technique study involving the most recent advances in materials science and electrochemistry has actually provided significant insight on the various processes occurring in cells with enhanced electrochemical behavior, thus paving the way to further improving the electrode performance. The characterization has shown that the pristine materials have microstructural characteristics depending on the metal additive which directly affect the reaction kinetics. Notably, tin is effectually embedded into the sulfur particles to form nanocomposite clusters, thereby leading to a higher electrode charge transfer, while nickel easily segregates in metal clusters leading to lower rate capability. *Ex situ* analyses supported by X-ray computed tomography have revealed that the electrode undergoes a substantial microstructural reorganization during the first discharge/charge cycle in the cell, consisting in a gradual migration of sulfur (i) towards the current collector bulk and (ii) close to the electron-conducting metal centers, as clearly shown by the supplementary movies provided herein (Movies S1-S4) which we warmly invite to analyze in sequence. We therefore suggest that both the conductive carbon-cloth electrode support and the metal centers may act as preferred sites for sulfur electrodeposition upon charge. Such a process leads to a massive loss of crystallinity of the sulfur phase along with a decrease of the average particle size. The observed electrode rearrangements are reflected into a shift of the potential and a remarkable drop of the electrode/electrolyte interphase

resistance, likely owing to the improved electric contact of newly electrodeposited sulfur. Meanwhile, Li/S cells using S-Sn and S-Ni electrodes exhibit a cycling behavior at the various currents in full agreement with the microstructure. In detail, the former material exhibits a higher rate capability likely due to the more homogenous mixing between sulfur and Sn particles, ensuring  $560 \text{ mAh gs}^{-1}$  at a 5C rate, while the latter delivers higher capacity at lower current rates, that is, from 1390 to 740  $\text{mAh gs}^{-1}$  within the range from C/3 to 3C ( $1\text{C} = 1675 \text{ mAh gs}^{-1}$ ). Hence, reversible sulfur conversion at about 2.2 V vs  $\text{Li}^+/\text{Li}$  with coulombic efficiency close to 100% and capacity retention of about 70% have been demonstrated in charge/discharge measurements upon 300 cycles.

Our results provide possible new research directions for the Li/S battery science, suggesting an alternative way to the sulfur confinement in carbonaceous matrices to prevent the lithium polysulfide dissolution. The study suggests the crucial role of the metal clusters and the electrode support for a fast conversion process by acting as sulfur electrodeposition centers. In this regard, we are confident that our novel approach may actually provide new insights on the sulfur electrode by suitably coupling three-dimensional imaging with advanced electrochemical measurements for strengthening the link between basic and applied research on lithium battery materials.

### **Acknowledgements**

This work was funded by the grant “Fondo di Ateneo per la Ricerca Locale (FAR) 2019”, University of Ferrara, and performed within the collaboration project “Accordo di Collaborazione Quadro 2015” between University of Ferrara (Department of Chemical and Pharmaceutical Sciences) and Sapienza University of Rome (Department of Chemistry). The authors acknowledge funding from EPSRC (EP/N032888/1, EP/K005030/1). PRS acknowledges the support to the Royal Academy of Engineering (CiET1718/59).

## References

- 1 K. M. Abraham, *J. Phys. Chem. Lett.*, 2015, **6**, 830–844.
- 2 G. A. Elia, U. Ulissi, S. Jeong, S. Passerini and J. Hassoun, *Energy Environ. Sci.*, 2016, **9**, 3210–3220.
- 3 D. Di Lecce, R. Verrelli and J. Hassoun, *Green Chem.*, 2017, **19**, 3442–3467.
- 4 L. Lu, X. Han, J. Li, J. Hua and M. Ouyang, *J. Power Sources*, 2013, **226**, 272–288.
- 5 B. Scrosati and J. Garche, *J. Power Sources*, 2010, **195**, 2419–2430.
- 6 B. Scrosati, *J. Solid State Electrochem.*, 2011, **15**, 1623–1630.
- 7 I. Tsiropoulos, D. Tarvydas and N. Lebedeva, *Li-ion batteries for mobility and stationary storage applications – Scenarios for costs and market growth*, EUR 29440 EN, Publications Office of the European Union, Luxembourg, 2018.
- 8 L. Carbone, S. G. Greenbaum and J. Hassoun, *Sustain. Energy Fuels*, 2017, **1**, 228–247.
- 9 S. Chung and A. Manthiram, *Adv. Mater.*, 2019, **31**, 1901125.
- 10 B. Scrosati, J. Hassoun and Y.-K. Sun, *Energy Environ. Sci.*, 2011, **4**, 3287.
- 11 A. Manthiram, Y. Fu, S.-H. Chung, C. Zu and Y.-S. Su, *Chem. Rev.*, 2014, **114**, 11751–11787.
- 12 R. Fang, S. Zhao, Z. Sun, D.-W. Wang, H.-M. Cheng and F. Li, *Adv. Mater.*, 2017, **29**, 1606823.
- 13 M. R. Busche, P. Adelhelm, H. Sommer, H. Schneider, K. Leitner and J. Janek, *J. Power Sources*, 2014, **259**, 289–299.
- 14 S. Zhang, K. Ueno, K. Dokko and M. Watanabe, *Adv. Energy Mater.*, 2015, **5**, 1500117.
- 15 Q. Pang, X. Liang, C. Y. Kwok and L. F. Nazar, *Nat. Energy*, 2016, **1**, 16132.
- 16 L. Carbone, T. Coneglian, M. Gobet, S. Munoz, M. Devany, S. Greenbaum and J. Hassoun, *J. Power Sources*, 2018, **377**, 26–35.
- 17 M. Li, W. Wahyudi, P. Kumar, F. Wu, X. Yang, H. Li, L.-J. Li and J. Ming, *ACS Appl. Mater. Interfaces*, 2017, **9**, 8047–8054.

- 18 A. Benítez, D. Di Lecce, G. A. Elia, Á. Caballero, J. Morales and J. Hassoun, *ChemSusChem*, 2018, **11**, 1512–1520.
- 19 N. Moreno, A. Caballero, J. Morales, M. Agostini and J. Hassoun, *Mater. Chem. Phys.*, 2016, **180**, 82–88.
- 20 J. Kim, D. J. Lee, H. G. Jung, Y. K. Sun, J. Hassoun and B. Scrosati, *Adv. Funct. Mater.*, 2013, **23**, 1076–1080.
- 21 A. Manthiram, S.-H. Chung and C. Zu, *Adv. Mater.*, 2015, **27**, 1980–2006.
- 22 J.-J. Chen, R.-M. Yuan, J.-M. Feng, Q. Zhang, J.-X. Huang, G. Fu, M.-S. Zheng, B. Ren and Q.-F. Dong, *Chem. Mater.*, 2015, **27**, 2048–2055.
- 23 X. Wang, Y. Gao, J. Wang, Z. Wang and L. Chen, *Nano Energy*, 2015, **12**, 810–815.
- 24 Z. Wang, J. Liu, L. Sun, Y. Zhang, Q. Fu, H. Xie and H. Sun, *Chem. – A Eur. J.*, 2018, **24**, 14154–14161.
- 25 L. Zhang, P. Liang, X. Man, D. Wang, J. Huang, H. Shu, Z. Liu and L. Wang, *J. Phys. Chem. Solids*, 2019, **126**, 280–286.
- 26 Z. Li, Q. He, X. Xu, Y. Zhao, X. Liu, C. Zhou, D. Ai, L. Xia and L. Mai, *Adv. Mater.*, 2018, **30**, 1804089.
- 27 J. Zheng, J. Tian, D. Wu, M. Gu, W. Xu, C. Wang, F. Gao, M. H. Engelhard, J.-G. Zhang, J. Liu and J. Xiao, *Nano Lett.*, 2014, **14**, 2345–2352.
- 28 Y.-S. Su and A. Manthiram, *Electrochim. Acta*, 2012, **77**, 272–278.
- 29 V. Marangon and J. Hassoun, *Energy Technol.*, 2019, **7**, 1900081.
- 30 M. Jeong, S. Ahn, T. Yokoshima, H. Nara, T. Momma and T. Osaka, *Nano Energy*, 2016, **28**, 51–62.
- 31 A. Sivashanmugam, T. P. Kumar, N. G. Renganathan, S. Gopukumar, M. Wohlfahrt-Mehrens and J. Garche, *J. Power Sources*, 2005, **144**, 197–203.
- 32 F. Croce, A. D' Epifanio, J. Hassoun, A. Deptula, T. Olczac and B. Scrosati, *Electrochem. Solid-State Lett.*, 2002, **5**, A47–A50.

- 33 Z. Zhao, D. Qin, S. Wang, G. Chen and Z. Li, *Electrochim. Acta*, 2014, **127**, 123–131.
- 34 H. Kim, H.-D. Lim, J. Kim and K. Kang, *J. Mater. Chem. A*, 2014, **2**, 33–47.
- 35 C. Tan, T. M. M. Heenan, R. F. Ziesche, S. R. Daemi, J. Hack, M. Maier, S. Marathe, C. Rau, D. J. L. Brett and P. R. Shearing, *ACS Appl. Energy Mater.*, 2018, **1**, 5090–5100.
- 36 T. M. M. Heenan, J. J. Bailey, X. Lu, J. B. Robinson, F. Iacoviello, D. P. Finegan, D. J. L. Brett and P. R. Shearing, *Fuel Cells*, 2017, **17**, 75–82.
- 37 D. Di Lecce, S. Levchenko, F. Iacoviello, D. J. L. Brett, P. R. Shearing and J. Hassoun, *ChemSusChem*, 2019, **12**, 3550 – 3561.
- 38 B. A. Boukamp, *Solid State Ionics*, 1986, **20**, 31–44.
- 39 B. Boukamp, *Solid State Ionics*, 1986, **18–19**, 136–140.
- 40 D. Di Lecce, R. Verrelli and J. Hassoun, *Electrochim. Acta*, 2016, **220**, 384–390.
- 41 D. Di Lecce, D. Campanella and J. Hassoun, *J. Phys. Chem. C*, 2018, **122**, 23925–23933.
- 42 A. Ševčík, *Collect. Czechoslov. Chem. Commun.*, 1948, **13**, 349–377.
- 43 J. E. B. Randles, *Trans. Faraday Soc.*, 1948, **44**, 327–338.
- 44 B. Münch and L. Holzer, *J. Am. Ceram. Soc.*, 2008, **91**, 4059–4067.
- 45 Q. Wang, D.-A. Zhang, Q. Wang, J. Sun, L.-L. Xing and X.-Y. Xue, *Electrochim. Acta*, 2015, **173**, 476–482.
- 46 S. Yamada, M. Fujiwara and M. Kanda, *J. Power Sources*, 1995, **54**, 209–213.
- 47 D. Avellaneda, I. Sánchez-Orozco, J. A. A. Martínez, S. Shaji and B. Krishnan, *Mater. Res. Express*, 2018, **6**, 016409.
- 48 Y. Gao, L. Wang, W. Zhang, X. Yang, Y. Ma, J. Shao and Y. Li, *Electrochim. Acta*, 2016, **201**, 260–267.
- 49 B. Meyer, *Chem. Rev.*, 1976, **76**, 367–388.
- 50 J. Hassoun, G. Derrien, S. Panero and B. Scrosati, *Adv. Mater.*, 2008, **20**, 3169–3175.
- 51 Y. Hou, H. Kondoh, T. Ohta and S. Gao, *Appl. Surf. Sci.*, 2005, **241**, 218–222.
- 52 C. Barchasz, F. Molton, C. Duboc, J.-C. Leprière, S. Patoux and F. Alloin, *Anal. Chem.*,

- 2012, **84**, 3973–3980.
- 53 S. Waluś, C. Barchasz, R. Bouchet, J.-C. Leprêtre, J.-F. Colin, J.-F. Martin, E. Elkaïm, C. Baecht and F. Alloin, *Adv. Energy Mater.*, 2015, **5**, 1500165.
- 54 D. Di Lecce, V. Marangon, A. Benítez, Á. Caballero, J. Morales, E. Rodríguez-Castellón and J. Hassoun, *J. Power Sources*, 2019, **412**, 575–585.
- 55 Q. Wang, J. Zheng, E. Walter, H. Pan, D. Lv, P. Zuo, H. Chen, Z. D. Deng, B. Y. Liaw, X. Yu, X. Yang, J.-G. Zhang, J. Liu and J. Xiao, *J. Electrochem. Soc.*, 2015, **162**, A474–A478.
- 56 L. Carbone, J. Peng, M. Agostini, M. Gobet, M. Devany, B. Scrosati, S. Greenbaum and J. Hassoun, *ChemElectroChem*, 2017, **4**, 209–215.
- 57 A. Benítez, D. Di Lecce, Á. Caballero, J. Morales, E. Rodríguez-Castellón and J. Hassoun, *J. Power Sources*, 2018, **397**, 102–112.
- 58 H. Kim, J. Lee, H. Ahn, O. Kim and M. J. Park, *Nat. Commun.*, 2015, **6**, 7278.
- 59 J. Zhu, E. Yildirim, K. Aly, J. Shen, C. Chen, Y. Lu, M. Jiang, D. Kim, A. E. Tonelli, M. A. Pasquinelli, P. D. Bradford and X. Zhang, *J. Mater. Chem. A*, 2016, **4**, 13572–13581.
- 60 A. Benítez, A. Caballero, J. Morales, J. Hassoun, E. Rodríguez-Castellón and J. Canales-Vázquez, *Nano Res.*, 2019, **12**, 759–766.
- 61 H. Shin, M. Agostini, I. Belharouak, J. Hassoun and Y.-K. Sun, *Carbon N. Y.*, 2016, **96**, 125–130.
- 62 C.-H. Liu, T.-H. Ko, W.-S. Kuo, H.-K. Chou, H.-W. Chang and Y.-K. Liao, *J. Power Sources*, 2009, **186**, 450–454.
- 63 J. Hassoun, Y. K. Sun and B. Scrosati, *J. Power Sources*, 2011, **196**, 343–348.
- 64 L. Carbone, R. Verrelli, M. Gobet, J. Peng, M. Devany, B. Scrosati, S. Greenbaum and J. Hassoun, *New J. Chem.*, 2016, **40**, 2935–2943.
- 65 L. Zielke, C. Barchasz, S. Waluś, F. Alloin, J.-C. Leprêtre, A. Spetl, V. Schmidt, A. Hilger, I. Manke, J. Banhart, R. Zengerle and S. Thiele, *Sci. Rep.*, 2015, **5**, 10921.
- 66 G. Tonin, G. Vaughan, R. Bouchet, F. Alloin, M. Di Michiel, L. Boutafa, J.-F. Colin and C.

- Barchasz, *Sci. Rep.*, 2017, **7**, 2755.
- 67 F. Sun, M. Osenberg, K. Dong, D. Zhou, A. Hilger, C. J. Jafta, S. Risse, Y. Lu, H. Markötter and I. Manke, *ACS Energy Lett.*, 2018, **3**, 356–365.
- 68 H. Yuan, H.-J. Peng, B.-Q. Li, J. Xie, L. Kong, M. Zhao, X. Chen, J.-Q. Huang and Q. Zhang, *Adv. Energy Mater.*, 2019, **9**, 1802768.
- 69 A. Benítez, Á. Caballero, E. Rodríguez-Castellón, J. Morales and J. Hassoun, *ChemistrySelect*, 2018, **3**, 10371–10377.
- 70 I. Raguzin, S. Choudhury, F. Simon, M. Stamm and L. Ionov, *Adv. Mater. Interfaces*, 2017, **4**, 1600811.
- 71 H.-J. Peng, J.-Q. Huang, X.-B. Cheng and Q. Zhang, *Adv. Energy Mater.*, 2017, **7**, 1700260.
- 72 D. Eroglu, K. R. Zavadil and K. G. Gallagher, *J. Electrochem. Soc.*, 2015, **162**, A982–A990.
- 73 S. Wei, Z. Li, K. Kimura, S. Inoue, L. Pandini, D. Di Lecce, Y. Tominaga and J. Hassoun, *Electrochim. Acta*, 2019, **306**, 85–95.
- 74 L. Carbone, M. Gobet, J. Peng, M. Devany, B. Scrosati, S. Greenbaum and J. Hassoun, *ACS Appl. Mater. Interfaces*, 2015, **7**, 13859–13865.
- 75 M. Shaibani, M. S. Mirshekarloo, R. Singh, C. D. Easton, M. C. D. Cooray, N. Eshraghi, T. Abendroth, S. Dörfler, H. Althues, S. Kaskel, A. F. Hollenkamp, M. R. Hill and M. Majumder, *Sci. Adv.*, 2020, **6**, eaay2757.
- 76 S.-H. Chung and A. Manthiram, *Electrochim. Acta*, 2013, **107**, 569–576.
- 77 H. Tang, S. Yao, M. Jing, X. Wu, J. Hou, X. Qian, D. Rao, X. Shen, X. Xi and K. Xiao, *Electrochim. Acta*, 2015, **176**, 442–447.
- 78 G. Babu, K. Ababtain, K. Y. S. Ng and L. M. R. Arava, *Sci. Rep.*, 2015, **5**, 8763.

## Table captions

**Table 1.** Electrode/electrolyte interphase resistances calculated through NLLS analyses of the impedance spectra of Figure 2c, recorded upon CV (see Figure 2a) of a Li | DOL:DME 1:1 w/w, 1 mol kg<sup>-1</sup> LiTFSI, 1 mol kg<sup>-1</sup> LiNO<sub>3</sub> | S:Sn 85:15 w/w cell. CV performed at a 0.1 mV s<sup>-1</sup> scan rate within the potential range from 1.8 to 2.8 V vs Li<sup>+</sup>/Li; EIS carried out at the OCV, after 1, 5 and 10 cycles by applying a 10 mV alternating signal within the frequency range from 500 kHz to 100 mHz. Measurement performed at 25 °C.

**Table 2.** Electrode/electrolyte interphase resistances calculated through NLLS analyses of the impedance spectra of Figure 2d, recorded upon CV (see Figure 2b) of a Li | DOL:DME 1:1 w/w, 1 mol kg<sup>-1</sup> LiTFSI, 1 mol kg<sup>-1</sup> LiNO<sub>3</sub> | S:Ni 85:15 w/w cell cell. CV performed at a 0.1 mV s<sup>-1</sup> scan rate within the potential range from 1.8 to 2.8 V vs Li<sup>+</sup>/Li; EIS carried out at the OCV, after 1, 5 and 10 cycles by applying a 10 mV alternating signal within the frequency range from 500 kHz to 100 mHz. Measurement performed at 25 °C.

## Figure captions

**Figure 1.** Electron and X-ray microscopy study of the composite powders. In detail: **(a-b)** SEM images of **(a)** S:Sn 85:15 w/w and **(d)** S:Ni 85:15 w/w (insets show magnifications), and **(b-c, e-f)** corresponding EDX elemental maps of **(b, e)** sulfur, **(c)** tin and **(f)** nickel; **(g, k)** TEM images of **(g)** S:Sn 85:15 w/w and **(k)** S:Ni 85:15 w/w (insets show the corresponding SAED patterns); **(h-j, l-n)** X-ray nano-CT study of **(h-j)** S:Sn 85:15 w/w and **(l-n)** S:Ni 85:15 w/w in terms of **(h, l)** slice extracted in the yz plane (X-ray attenuation depicted through a grayscale), **(i, m)** corresponding three-phase segmentation (S: yellow; Sn: blue; Ni: green; exterior: black), and **(j, n)** segmented volume rendering including and (inset) excluding the S phase (S: yellow; Sn: blue; Ni: green). Voxel size:  $63 \times 63 \times 63 \text{ nm}^3$ . Scans performed in X-ray absorption-contrast and large-field-of-view ( $65 \text{ }\mu\text{m}$ ) modes, by taking 1601 projections through  $180^\circ$ .

**Figure 2.** **(a-b)** CV profiles (potential range:  $1.8 - 2.8 \text{ V vs Li}^+/\text{Li}$ ; scan rate:  $0.1 \text{ mV s}^{-1}$ ) and **(c, d)** corresponding Nyquist plots (magnification in inset) of EIS measurements performed at the OCV, after 1, 5 and 10 cycles (frequency range, *i.e.*,  $\omega$ :  $500 \text{ kHz} - 100 \text{ mHz}$ ; signal amplitude:  $10 \text{ mV}$ ) for Li | DOL:DME 1:1 w/w,  $1 \text{ mol kg}^{-1} \text{ LiTFSI}$ ,  $1 \text{ mol kg}^{-1} \text{ LiNO}_3$  | cathode cells using the **(a, c)** S:Sn 85:15 w/w and **(b, d)** S:Ni 85:15 w/w electrodes. **(e, f)** CV profiles at various scan rates ( $0.05, 0.1, 0.15, 0.2$  and  $0.25 \text{ mV s}^{-1}$ ; potential range:  $1.8 - 2.8 \text{ V vs Li}^+/\text{Li}$ ; top panels) of Li | DOL:DME 1:1 w/w,  $1 \text{ mol kg}^{-1} \text{ LiTFSI}$ ,  $1 \text{ mol kg}^{-1} \text{ LiNO}_3$  | cathode cells using the **(e)** S:Sn 85:15 w/w and **(f)** S:Ni 85:15 w/w electrodes and corresponding  $\text{Li}^+$  diffusion coefficients ( $D$ ; bottom panels) according to Randles-Sevcik equation.<sup>42,43</sup> Measurements performed at  $25 \text{ }^\circ\text{C}$ .

**Figure 3.** XRD and X-ray micro-CT analysis of S:Sn 85:15 w/w and S:Ni 85:15 w/w electrode samples before and after cycling at a constant current of  $C/3$  ( $1C = 1675 \text{ mA gs}^{-1}$ ) in Li | DOL:DME 1:1 w/w,  $1 \text{ mol kg}^{-1} \text{ LiTFSI}$ ,  $0.4 \text{ mol kg}^{-1} \text{ LiNO}_3$  | cathode cells (voltage range:  $1.9 - 2.8 \text{ V vs Li}^+/\text{Li}$ ). **(a, b)** XRD patterns of **(a)** S:Sn 85:15 w/w and **(b)** S:Ni 85:15 w/w electrodes collected at the pristine condition, and *ex situ* after 1 and 10 discharge/charge cycles; reference data for elemental sulfur

(yellow bars, ICSD # 27840), metallic tin (blue bars, ICSD # 40038) and metallic nickel (green bars, ICSD # 672759). **(c-j)** X-ray micro-CT analysis of **(c-d, g-h)** S:Sn and **(e-f, i-j)** S:Ni electrode samples **(c-f)** before and **(g-j)** after 1 discharge/charge cycle in terms of **(c, e, g, i)** volume rendering using a grayscale representation (X-ray attenuation depicted through a grayscale) and **(d, f, h, j)** slice extracted in plane orthogonal to the electrode surface with corresponding segmentation (S: yellow; Sn: blue; S-Sn intimate mixture: light blue; Ni: green; S-Ni intimate mixture: light green; carbon/binder/carbon-cloth: gray; exterior: black). Voxel size: from 288×288×288 to 373×373×373 nm<sup>3</sup>; field of view: from about 570 to about 730 μm. Scan performed by taking 1601 projections through 360°.

**Figure 4.** X-ray micro-CT analysis of **(a-b, e-f)** S:Sn 85:15 w/w and **(c-d, g-h)** S:Ni 85:15 w/w electrode samples **(a-d)** before and **(e-g)** after 1 discharge/charge cycle at a constant current of C/3 (1C = 1675 mA gs<sup>-1</sup>) in Li | DOL:DME 1:1 w/w, 1 mol kg<sup>-1</sup> LiTFSI, 0.4 mol kg<sup>-1</sup> LiNO<sub>3</sub> | cathode cells (voltage range: 1.9 – 2.8 V vs Li<sup>+</sup>/Li). In detail: **(a, c, e, g)** segmented volume rendering (S: yellow; Sn: blue; S-Sn intimate mixture: light blue; Ni: green; S-Ni intimate mixture: light green; carbon/binder/carbon-cloth: gray) and **(b, d, f, h)** discrete particle size distribution<sup>44</sup> (PSD) of the S and S-metal domains as determined by analysis of the micro-CT datasets. Voxel size: from 288×288×288 to 373×373×373 nm<sup>3</sup>; field of view: from about 570 to about 730 μm. Scan performed by taking 1601 projections through 360°.

**Figure 5.** **(a-b)** Voltage profiles and **(c-d)** corresponding cycling trends with coulombic efficiency (right y-axis) of galvanostatic measurements performed on Li | DOL:DME 1:1 w/w, 1 mol kg<sup>-1</sup> LiTFSI, 1 mol kg<sup>-1</sup> LiNO<sub>3</sub> | cathode cells employing the **(a, c)** S:Sn 85:15 w/w and **(b, d)** S:Ni 85:15 w/w composites. Tests performed at C/3, 1C, 2C and 3C current rates (1C = 1675 mA gs<sup>-1</sup>) within the voltage ranges of 1.9 – 2.8 V for C/3 and 1C, and of 1.8 – 2.8 V for 2C and 3C. Specific capacity referred to the sulfur mass. Measurements performed at 25 °C.

**Figure 6. (a-b)** Rate capability test on Li | DOL:DME 1:1 w/w, 1 mol kg<sup>-1</sup> LiTFSI, 1 mol kg<sup>-1</sup> LiNO<sub>3</sub> | cathode cells employing the **(a)** S:Sn 85:15 w/w and **(b)** S:Ni 85:15 w/w composites at C/10, C/8, C/5, C/3, C/2, 1C, 2C, 3C, 4C, 5C, 8C and 10C (1C = 1675 mA gs<sup>-1</sup>). Voltage range: 1.9 – 2.8 V from C/10 to C/2 and 1.8 – 2.8 V from 1C to 10C. Specific discharge capacity referred to the sulfur mass. **(c-d)** Steady-state voltage profile and discharge capacity trend upon the first 10 discharge-charge cycles (inset) of Li | DOL:DME 1:1 w/w, 1 mol kg<sup>-1</sup> LiTFSI, 1 mol kg<sup>-1</sup> LiNO<sub>3</sub> | cathode cells employing the **(c)** S:Sn 85:15 w/w and **(d)** S:Ni 85:15 w/w composites with a sulfur loading of 6.8 and 6.3 mg cm<sup>-2</sup>, respectively. Tests performed at a constant current of C/20 (1C = 1675 mA gs<sup>-1</sup>) within the voltage range of 1.9 – 2.8 V. Discharge specific capacity (bottom x-axis in the main panels and left y-axis in insets) referred to the sulfur mass (mAh gs<sup>-1</sup>); discharge areal capacity (top x-axis in the main panels and right y-axis in insets) referred to the electrode geometric area (1.54 cm<sup>2</sup>, mAh cm<sup>-2</sup>). **(e)** Cycling trends with coulombic efficiency of galvanostatic measurements performed on Li | DEGDME, 1 mol kg<sup>-1</sup> LiTFSI, 1 mol kg<sup>-1</sup> LiNO<sub>3</sub> | cathode cells employing the S:Sn 85:15 w/w and S:Ni 85:15 w/w composites. Tests performed at a 1C rate (1C = 1675 mA gs<sup>-1</sup>) within the voltage range of 1.8 – 2.8 V. Specific capacity referred to the sulfur mass. All the measurements were performed at 25 °C.

Cell condition	Equivalent circuit	$R_1$ ( $\Omega$ )	$R_2$ ( $\Omega$ )	$R_1 + R_2$ ( $\Omega$ )	$\chi^2$
OCV	$R_e(R_1Q_1)(R_2Q_2)$	$19.9 \pm 0.7$	$5.7 \pm 1.6$	$26 \pm 2$	$2.0 \times 10^{-4}$
1 CV cycle	$R_e(R_1Q_1)(R_2Q_2)Q_3$	$1.04 \pm 0.06$	$0.88 \pm 0.14$	$1.92 \pm 0.2$	$9.9 \times 10^{-5}$
5 CV cycles	$R_e(R_1Q_1)(R_2Q_2)Q_3$	$1.78 \pm 0.05$	$0.27 \pm 0.06$	$2.05 \pm 0.11$	$8.3 \times 10^{-5}$
10 CV cycles	$R_e(R_1Q_1)(R_2Q_2)Q_3$	$2.22 \pm 0.05$	$0.16 \pm 0.05$	$2.38 \pm 0.10$	$5.3 \times 10^{-5}$

**Table 1**

Cell condition	Equivalent circuit	$R_1$ ( $\Omega$ )	$R_2$ ( $\Omega$ )	$R_1 + R_2$ ( $\Omega$ )	$\chi^2$
OCV	$R_e(R_1Q_1)$	$137.5 \pm 0.9$	/	$137.5 \pm 0.9$	$5.2 \times 10^{-4}$
1 CV cycle	$R_e(R_1Q_1)(R_2Q_2)Q_3$	$1.22 \pm 0.04$	$0.80 \pm 0.08$	$2.02 \pm 0.12$	$5.5 \times 10^{-5}$
5 CV cycles	$R_e(R_1Q_1)(R_2Q_2)Q_3$	$1.88 \pm 0.05$	$0.36 \pm 0.09$	$2.24 \pm 0.14$	$6.6 \times 10^{-5}$
10 CV cycles	$R_e(R_1Q_1)(R_2Q_2)Q_3$	$2.25 \pm 0.05$	$0.24 \pm 0.05$	$2.49 \pm 0.10$	$5.9 \times 10^{-5}$

**Table 2**

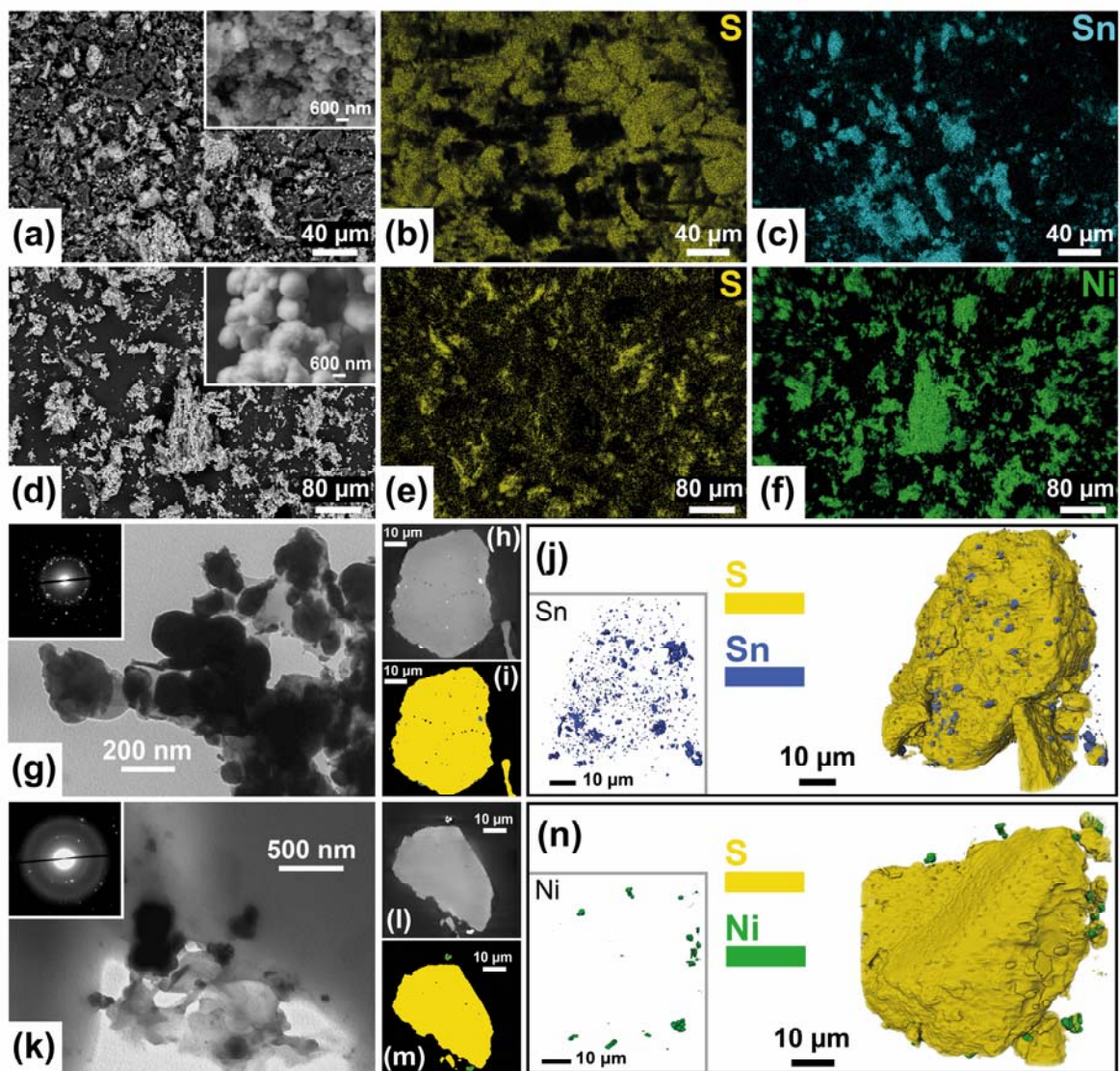


Figure 1

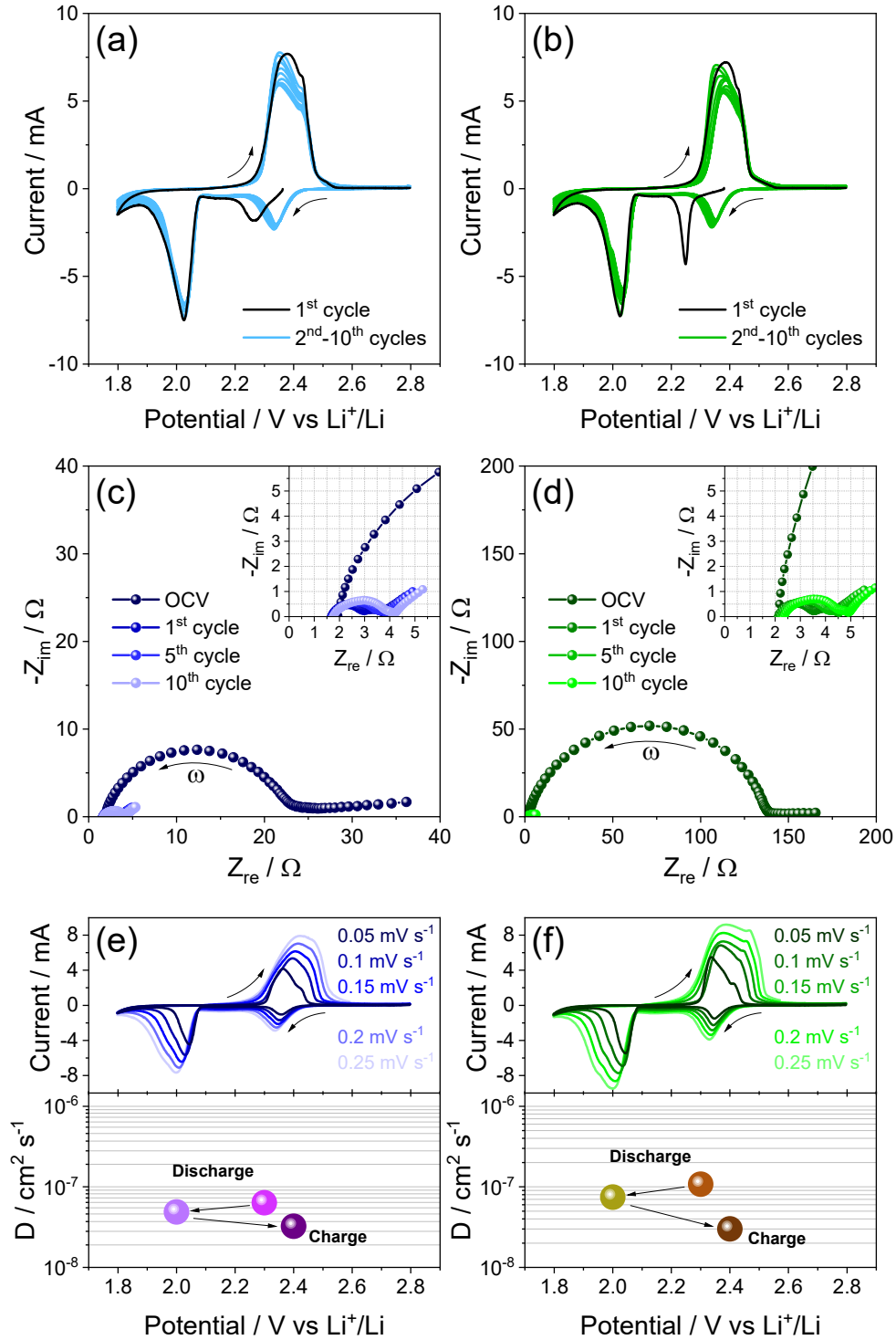


Figure 2

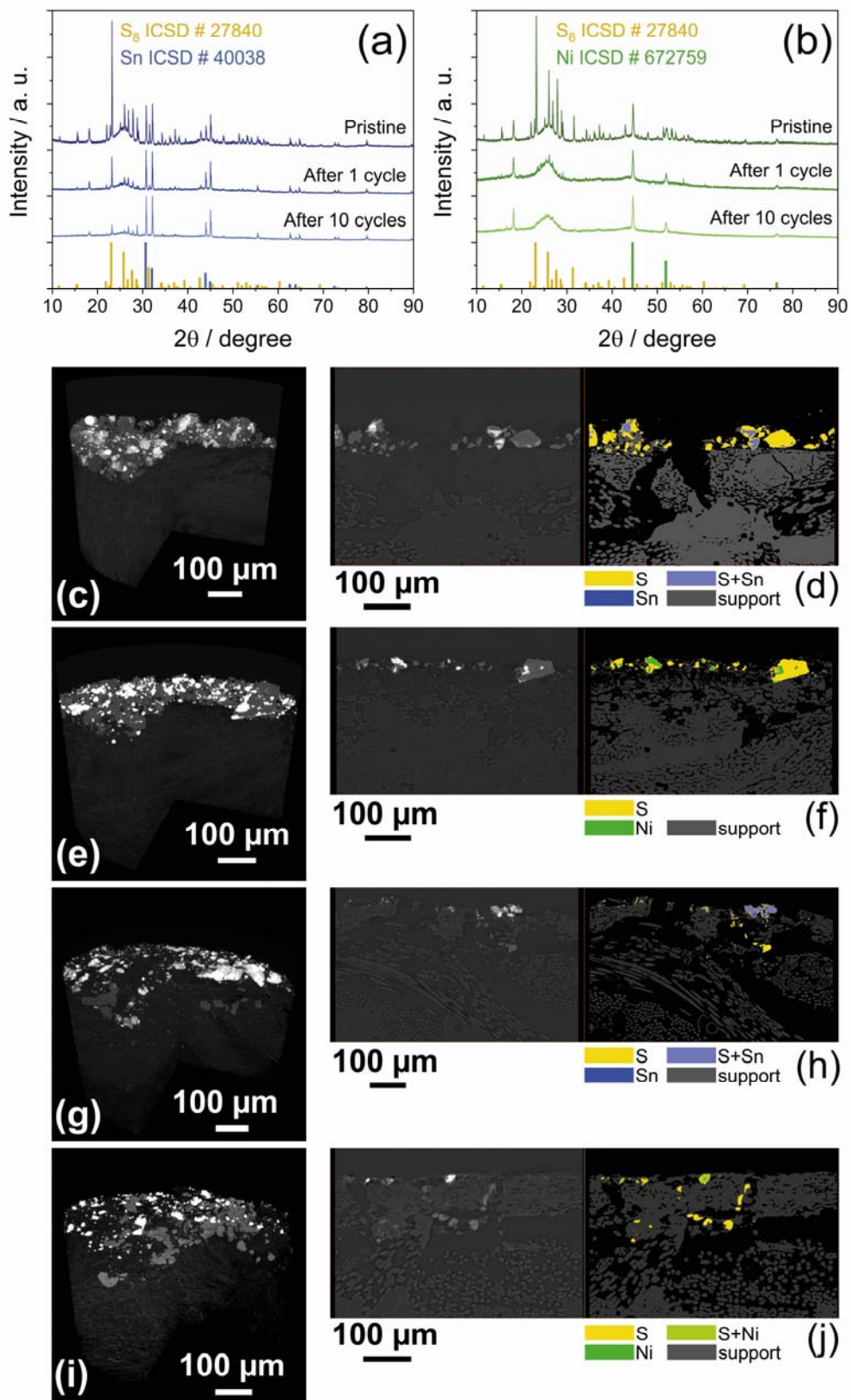


Figure 3

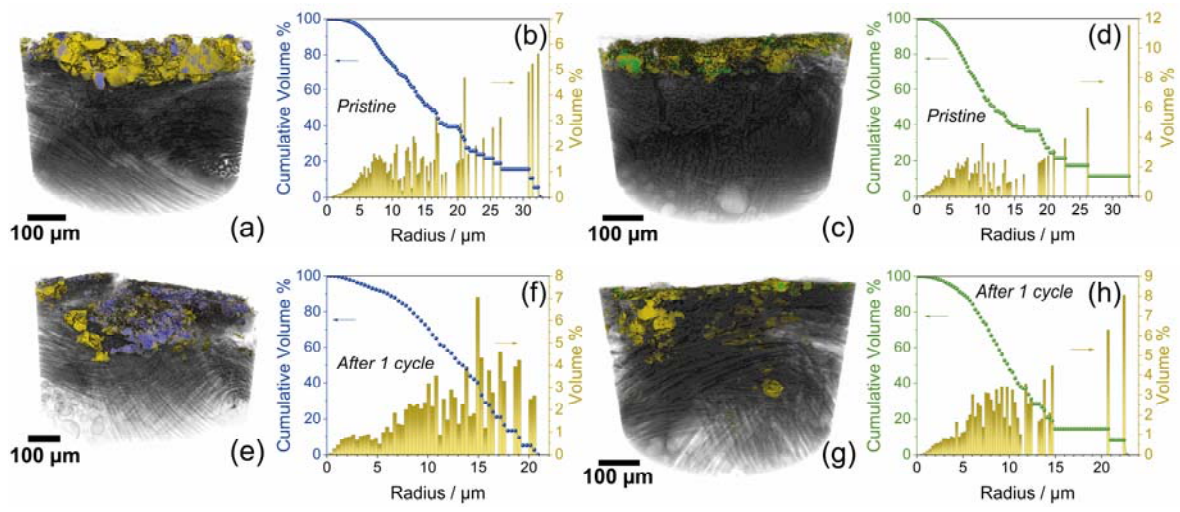


Figure 4

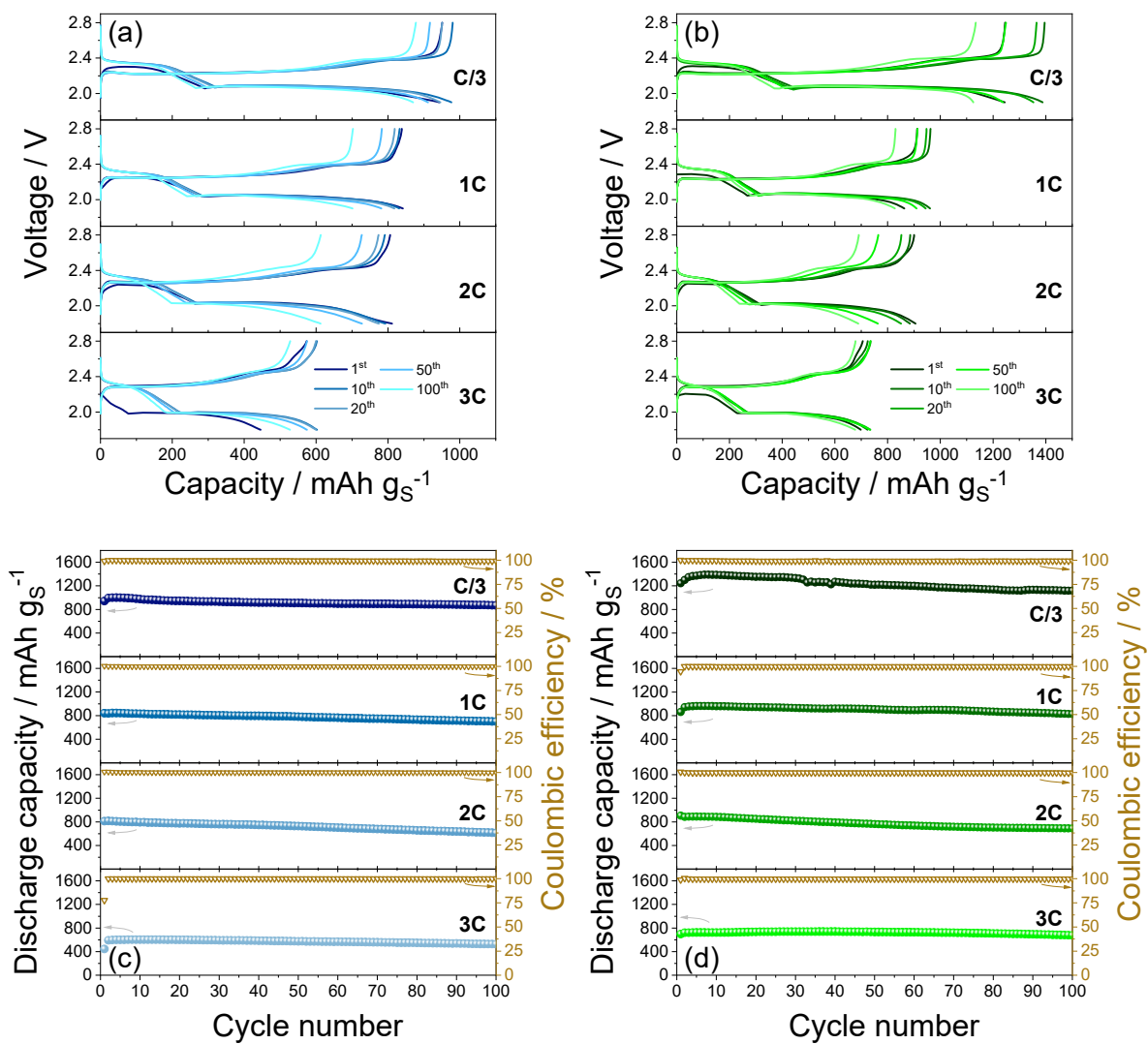


Figure 5

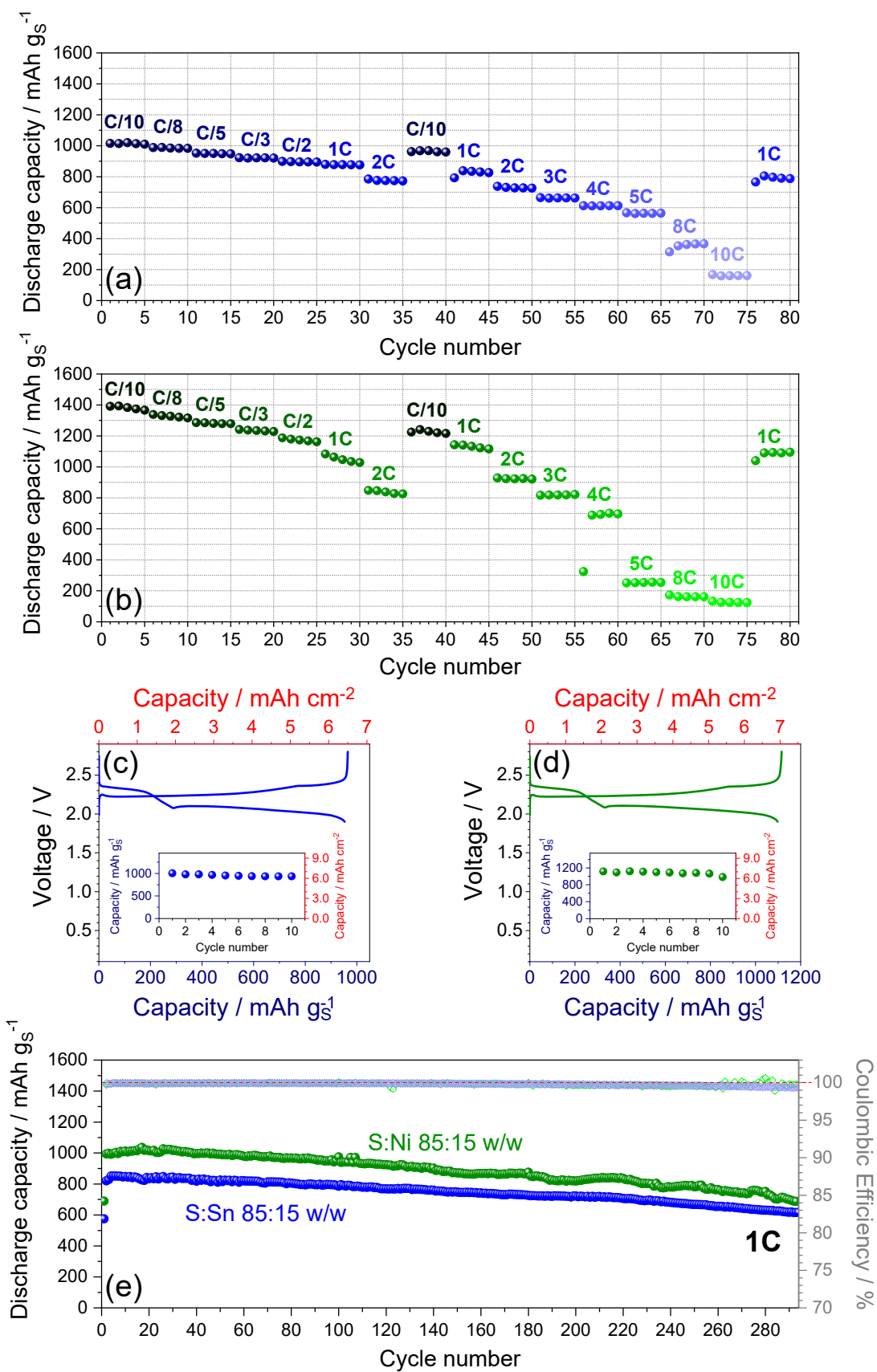


Figure 6

## Table of contents

X-ray tomography and electrochemistry shed light on a novel approach to prepare high-performance cathodes for lithium-sulfur batteries. Metal nanoparticles promote beneficial microstructural reorganizations in the cathode during the cycling process.

